ELECTRONIC, MAGNETIC AND TRANSPORT PROPERTIES OF GRAPHENE QUANTUM DOTS WITH CHARGED IMPURITIES

A Dissertation Submitted to
the Graduate School of Engineering and Sciences of
İzmir Institute of Technology
in Partial Fulfillment of the Requirements for the Degree of

DOCTOR OF PHILOSOPHY

in Physics

by
Mustafa POLAT

December 2020
İzmir

ACKNOWLEDGMENTS

ABSTRACT

ELECTRONIC, MAGNETIC AND TRANSPORT PROPERTIES OF GRAPHENE QUANTUM DOTS WITH CHARGED IMPURITIES

In this thesis, electronic, magnetic, and transport properties of armchair edged hexagonal and zigzag edged triangular graphene quantum dots (GQDs) are investigated in the presence of charged impurities. In this manner, a special attention has been paid to the Coulomb impurity problem in these structures. The collapse of the wave functions starting from the $1S_{1/2}$ state is studied in the presence of not only the Coulomb impurity but also in the presence of a Coulomb charged vacancy with the help of tight-binding and extended mean-field Hubbard (MFH) models. Here, we report an interaction induced renormalization of the critical coupling constant (β_c). In addition, our results suggest that the induced charge for the interacting fermions is smaller than that of the non-interacting fermions. Furthermore, the transport coefficients reveal two different characteristics of the subcritical ($\beta < \beta_c$) and supercritical ($\beta > \beta_c$) regimes. As for the charged vacancy, the bare carbon vacancy induces a local magnetic moment in the hexagonal GQDs, but it is suppressed when the vacancy is charged with the subcritical Coulomb potential.

Except the pristine cases of the GQDs, we numerically study a Coulomb impurity problem for the interacting fermions restricted in disordered hexagonal GQDs. In the presence of randomly distributed lattice defects and spatial potential fluctuations induced by Gaussian impurities, the response of β_c for atomic collapse is mainly investigated by local density of states (LDOS) calculations within the MFH model. We find that both types of disorder cause an amplification of the critical threshold. As for the zigzag edged triangular GQDs, in the presence of the bare vacancy, we exactly obtain the spin splitting with the help of LDOS calculations in the energy spectrums, which are dominated by the edge states around the Fermi level. Similar to the hexagonal GQDs, if the vacancy is charged, the local magnetic moment disappears in these GQDs.

ÖZET

YÜKLÜ SAFSIZLIKLAR İÇEREN GRAFEN KUANTUM NOKTALARIN ELEKTRONİK, MANYETİK VE TAŞINIM ÖZELLİKLERİ

Bu tezde, koltuk kenarlı altıgen ve zikzak kenarlı üçgen grafen kuantum noktaların (GKN) elektronik, manyetik ve taşıma özellikleri yüklü safsızlıklar varlığında incelenmektedir. Bu manada, bu tür yapılarda Coulomb safsızlık problemine özel bir dikkat gösterilmiştir. Dalga fonksiyonlarının $1S_{1/2}$ durumundan başlayarak çöküşü, sadece bir Coulomb safsızlığı varlığında değil aynı zamanda yüklü bir boşluk varlığında da sıkı bağlanma ve genişletilmiş ortalama alan Hubbard (OAH) modelleri yardımıyla çalışılmıştır. Burada, kritik bağlanma sabitinin (β_c) etkileşim kaynaklı artışını rapor ediyoruz. Ek olarak, sonuçlarımız etkileşmeyen duruma kıyasla etkileşen fermiyonlar için indüklenen yükün azaldığını öngörmektedir. Dahası, taşıma katsayıları kritik altı ($\beta < \beta_c$) ve kritik üstü ($\beta > \beta_c$) rejimlerin iki farklı karakterini ortaya çıkartmaktadır. Yüklü karbon boşluğuna gelince, çıplak boşluk altıgen GKN'larda yerel bir manyetik moment meydana getirir, ancak çıplak boşluk kritik altı Coulomb potansiyeli ile yüklendiğinde yerel manyetik moment bastırılmaktadır.

Farklı büyüklükteki temiz GKN'ların haricinde, düzensiz altıgen GKN'lara sınırlandırılmış etkileşen fermiyonlar için Coulomb safsızlık problemi nümerik olarak incelenmektedir. Rastgele dağıtılmış örgü kusurları ve Gauss safsızlıklarının neden olduğu uzamsal potansiyel dalgalanmalar varlığında, β_c'ğin tepkisi genişletilmiş OAH modelindeki yerel durum yoğunluk (YDY) hesaplamaları ile araştırılmıştır. Her iki tür bozukluğunda kritik eşiğin yükselmesine neden olduğu gösterilmiştir. Zikzak kenarlı üçgen GKN'lara gelince, yüksüz boşluk varlığında, Fermi seviyesi civarında kenar durumları tarafından domine edilmiş enerji spektrumları içerisinde, YDY hesapları yardımıyla, spin ayrışması tam olarak bulunmuştur. Altıgen GKN'lara benzer şekilde, eğer boşluk yüklenirse, yerel manyetik momentin kaybolduğu gösterilmektedir.

To My Lovely Family . . .

TABLE OF CONTENTS

LIST OF FIGURES

LIST OF SYMBOLS

E_{gap} . . . . Band gap energy

β . . . . Coupling strength

β_c . . . . Critical coupling constant

Z . . . . Nuclear charge

Z_c . . . . Critical nuclear charge

α . . . . Fine structure constant

κ . . . . Dielectric constant

$\hbar$ . . . . Reduced Planck constant

c . . . . Speed of light

e . . . . Electron charge

j . . . . Total angular momentum number

t . . . . Hopping term

$\delta p(r)$ . . . . Induced charge density

Q . . . . Induced charge

a . . . . C-C distance

Ψ . . . . Wave function

H . . . . Hamiltonian

U . . . . On-site Coulomb repulsion term

V . . . . Off-site Coulomb repulsion term

$\hat{c}^\dagger$ . . . . Creation operator

$\hat{c}$ . . . . Annihilation operator

$\hat{n}$ . . . . Number operator

$\langle \hat{n} \rangle$ . . . . Expectation value of electron density

LIST OF ABBREVIATIONS

QED . . . . Quantum electrodynamics

TB . . . . Tight binding

2D . . . . Two dimensional

DP . . . . Dirac point

GQD . . . . Graphene quantum dot

QBS . . . . Quasi-bound state

STM . . . . Scanning tunneling microscopy

FL . . . . Fermi level

MFH . . . . Mean-field Hubbard

eV . . . . Electron volt

DOS . . . . Density of states

LDOS . . . . Local density of states

RPA . . . . Random phase approximation

CVD . . . . Chemical vapor deposition

CHAPTER 1

INTRODUCTION

Graphene with relativistic massless Dirac fermions is the perfect playground for testing the predictions of quantum electrodynamics (QED) such as the Klein tunneling (Katsnelson et al. (2006)) and the fractional quantum Hall effect (Bolotin et al. (2009)). Another one of these predictions is atomic collapse, which refers to as the spontaneous formation of electrons and positrons in the electrostatic field produced by a atomic nucleus. The single-atom-thick material allows one to observe atomic collapse with the help of experimentally accessible Coulomb impurities. In this thesis, we have examined atomic collapse in finite graphene samples. First, we will introduce the finite graphene samples, which have taken into consideration. Second, in this chapter, we will introduce the long-standing phenomenon of QED in graphene in more detail.

1.1. Graphene and Graphene Quantum Dots

Graphene consists of carbon atoms arranged in a honeycomb lattice with a carbon-carbon distance of a = 1.42 Å. Electronic configuration of carbon atoms is $1s^2 2s^2 2p^2$ in which the two $1s$ electrons are core electrons of the atoms, and which are irrespective of the conduction process. In this electron configuration, the remaining four electrons distribute themselves among the remaining four orbitals in which each orbital takes a single electron (Neto et al. (2009)). Actually, the three valance electrons in s, p_x, p_y orbitals form σ bonds between the carbon atoms by the sp^2 hybridization, oriented at 120° with respect to each other, which is responsible for the robustness of the lattice structure. The remaining single valance electrons in p$_z$ orbitals correspond to the π_z bonds, which are perpendicular to the graphene plane and determine the electronic properties of the lattice. Bravais lattice of graphene consists of two atoms, which are labelled as A and B in the unit cell, and the interaction between these two atoms leads to the formation of the valance (π) and conduction (π^*) bands. In the tight binding (TB) approximation, dispersion relation of graphene shows that the valance and conduction bands touch each

other at six points in the Brillouin zone, which indicates that graphene is a zero-band-gap semiconductor (Neto et al. (2009)), see Fig. 1.1(a)-(c). Graphene, as a two-dimensional (2D) allotrope of carbon, is of significant interest starting from its first experimental isolation (Novoselov et al. (2004)), since a novel sp^2-hybridized carbon network has significant physical properties (Neto et al. (2009)) as compared to other carbon allotropes. Starting from its experimental isolation from graphite, which is actually stacked layers of graphene sheets held together by the weak Van der Waals forces, most of the studies search a way to use graphene for the next generation devices. Significant physical properties such as high thermal conductivity, high electrical conductivity, high elasticity and flexibility render graphene a very studied material with great possibilities. As for the current literature, a great part of the electronic properties of graphene has been reviewed by Castro-Neto et al. (Neto et al. (2009)), transport properties by Das Sarma et al. (Sarma et al. (2011)), and many-body effects by Kotov et al. (Kotov et al. (2012)), Vozmedano et al. (Vozmediano and Guinea (2012)), and MacDonald et al. (MacDonald et al. (2012)). A broad range of topics related to graphene science can likewise be found in books, e.g., Katsnelson (Katsnelson and Iosifovich (2012)), Aoki et al. (Aoki and Dresselhaus (2013)), and Torres et al. (Torres et al. (2020)).
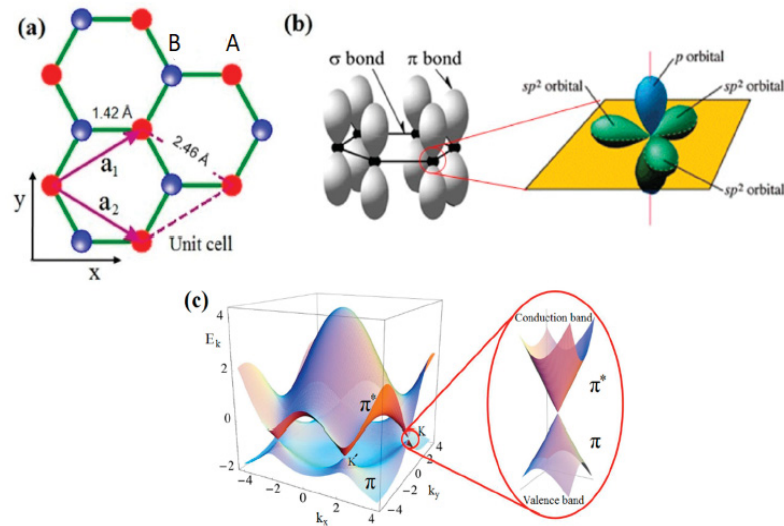
Figure 1.1. (a) Bravais lattice of graphene whose the lattice constant is 2.46 Å, (b) in-plane σ, which are consisting of the sp^2 hybridization, and out of plane π bonds in graphene, and (c) 3D dispersion relation of graphene shows the valance and conduction bands. Here, the inequivalent K and K' points is also shown (Source: (Yazdi et al. (2016)).

Since the single-atom-thick material is a semiconductor with a zero-energy band at the Dirac point (DP), the current can not be turned on/off. Furthermore, because of the Klein paradox and the zero band gap, it is hard to restrict Dirac fermions to an external electric field, which inhibits its application to transistors. It leads to another question: Can we take graphene as a beginning material and modify its electronic, magnetic, and transport properties by adjusting the size, the shape, and the kind of edge? Actually, by creating graphene quantum dots (GQDs) (Ponomarenko et al. (2008)), it is possible to engineer physical properties of graphene. In this manner, the GQDs have attracted increasing interest in material science (Güçlü et al. (2014)). By controlling the size of bulk graphene with the help of 0D GQDs, the energy gap can created, which can be tuned to a range of frequencies from terahertz to ultraviolet. In this way, the limited size of graphene can be turned into a semiconductor. Similarly, one can imagine designing a magnet and a laser by using these 0D carbon materials and making nanoscale quantum circuits consisting of the GQDs. Obtaining graphene nanostructures from single layer graphene brings about two stable edges, which are armchair and zigzag edges, and these edges can be described in such a way that the sublattice imbalance is preserved or not. These stable edges are responsible for the anti-ferromagnetic and ferromagnetic ground states in these finite samples. As we will show below, these two kinds of edge and the different shapes of the GQDs dictate a significant part of electronic and magnetic properties of these nanostructures.

The experimental manufacturing methodologies of the GQDs fall into two main categories, which are top-down and bottom-up techniques. Top-down technique refers to peeling of mass graphene-based materials, which is most generally graphite, to produce monolayer graphene. This technique requires deeper knowledge about the material in order to obtain the GQDs. In addition, the process may contain complex techniques including concentrated acids, solid oxidizing, and high temperatures. On the other hand, the bottom-up technique uses a combination of different particles with fragrant structures in order to produce the GQDs. In spite of its complexity, this technique provides an exact control of the morphology and size dispersion of the particles delivered (Bacon et al. (2014)). As a good example for the bottom-up technique, atomically precise π_z-extended triangular graphene quantum dots with zigzag edges were constructed via a precursor molecules (Su et al. (2019)).

Throughout this thesis, in the presence of experimentally relevant charged impurities, we will study the electronic magnetic, and transport properties of the hexagonal GQDs with armchair edges and the triangular GQDs with zigzag edges, which are illustrated in Fig. 1.2(a) and Fig. 1.2(b), respectively. In our numerical calculations, we obtained these GQDs by cutting from an infinite monolayer graphene. Such GQDs come to the fore with their size-dependent, edge-dependent, and shape-dependent intrinsic properties. For example, the hexagonal GQD with armchair edges has an energy gap, which corresponds to confined Dirac fermions (Güçlü et al. (2010)). This energy gap is inversely proportional to the number of atoms of the hexagonal GQDs. These GQDs are anti-ferromagnetic due to their armchair edges, and transmission coefficients of them are also inversely proportional to the number of atoms (Polat et al. (2020)). As for the triangular GQDs with zigzag edges, they have a net magnetic moment in their ground states due to the spin-polarized edge states (Su et al. (2019)). On the other hand, as a motivation for this thesis, charged impurities in these QDs can be used to adjust these intrinsic properties for many purposes. As an example, when a Coulomb impurity is placed at the center of the hexagonal GQDs, and if the value of coupling strength between the GQD and the Coulomb impurity exceeds a critical threshold, we found that the lowest energy electron state of the hexagonal GQD turns into a quasi-bound state (QBS), which corresponds to the first supercritical state, i.e., the $1S_{1/2}$ state, of the Coulomb impurity. This is known as the graphene version of atomic collapse in the current literature, and similarly, many supercritical states can bound to the Coulomb impurity, depending on the value of the coupling strength (Shytov et al. (2007a)). Such a formation of the quasi-bound state in the QDs results in a sudden downshift in the transmission peaks, as demonstrated by our previous work (Polat et al. (2020)). In addition to this special effect, it is well-known that the local magnetic moment, i.e., spin-splitting in the energy spectrum between spin-up and spin-down fermions, in graphene can be induced by introducing a bare vacancy, but it can be adjusted by charging the vacancy with the Coulomb potential (Polat et al. (2020)). On the other hand, the valley splittings or orbital splitting in the electron and hole channels continue to exist, as discussed by our previous study (Polat et al. (2020)). As for other impurities in the GQDs, we also studied the effect of electron-hole puddles induced by Gaussian impurities and the lattice distortions induced by point vacancies on atomic collapse with the help of local density of state calculations within

the extended mean field Hubbard model (Polat and Güçlü (2020)). These calculations simply show us that atomic collapse can also be observed in a defect-rich samples such as hydrogenated graphene (Polat and Güçlü (2020)). In short, by modifying the structure of a 2D lattice via experimentally relevant impurities, electronic, magnetic and transport properties of the GQDs can be adjusted, and which can be used to create new type of devices in the near future.
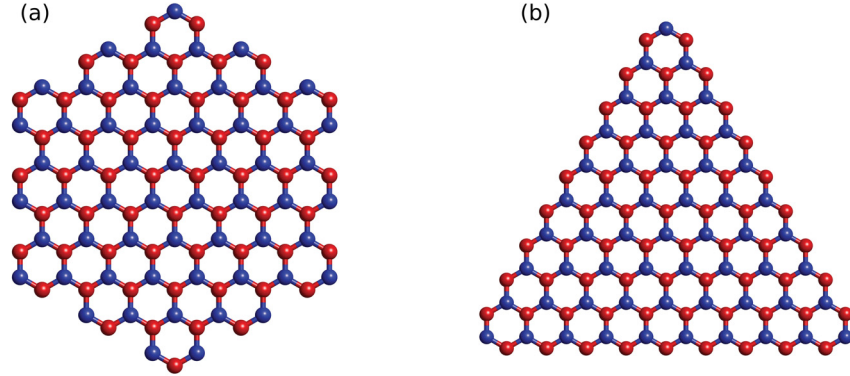
Figure 1.2. An illustration of the hexagonal GQD with armchair edges in (a) and the triangular GQD with zigzag edges in (b), which are under examination in this thesis. A and B sublattice atoms are represented by red and blue filled hard spheres, respectively.

For these GQDs, the energy spectrums within the TB approximation are given below in Fig. 1.3(a)-(d). Here, we restrict ourselves only to the nearest neighbour interaction of the lattice sites. For hexagonal GQDs consisting of 114 atoms, the energy spectrum has a clear band gap, as shown in Fig. 1.3(a), and the first states above and below the Fermi level (FL) are doubly degenerate, as shown in the zoomed portion of the energy spectrum [Fig. 1.3(a)]. As for the triangular GQDs with zigzag edge, there is an localized edge states within the energy spectrum, and such states are responsible for the ferromagnetism in these GQDs [Fig. 1.3(c)-(d)]. Similarly, we have two doubly degenerate states around the FL for the triangular GQDs.

We will study that the effects of charged impurities on the electronic and magnetic properties when they are intentionally introduced to these structures. In the next, starting from the prediction of the QED, we will examine the current literature findings related to the Coulomb impurity, and the equivalence of this phenomenon is experimentally reachable in bulk graphene (Wang et al. (2013)). In this manner, the Coulomb impurity
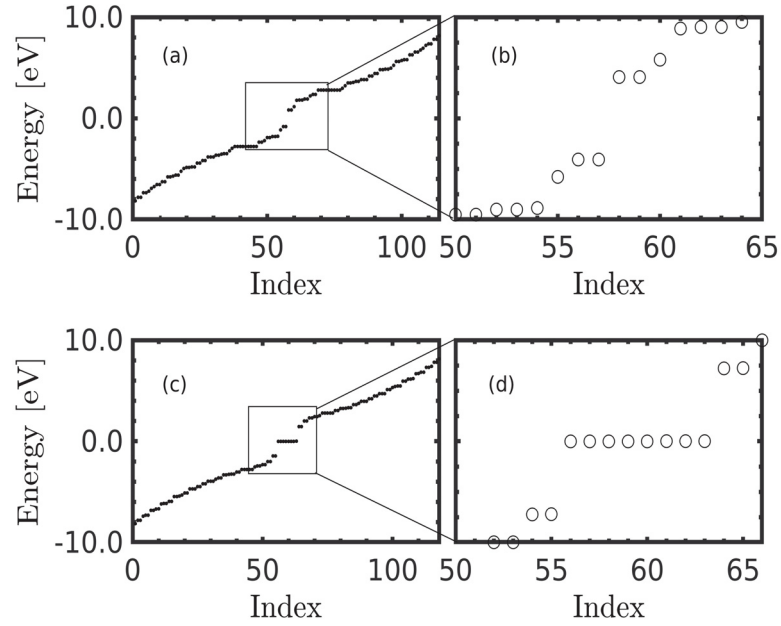
Figure 1.3. (a) shows the energy spectrum of the hexagonal GQD consisting of 114 atoms, (b) belongs to a zoomed portion of the same spectrum around the Fermi level, (c) and (d) show the energy spectrum of the zigzag-edged triangular GQDs consisting of 118 atoms.

problem paves the way for observing of the collapse resonances in graphene with the help of local density of state measurements.

1.2. Atomic Collapse in Quantum Electrodynamics

Rutherford's model has revealed the problem related to the stability of the atoms. The electron rotating around the nucleus falls to the center by losing its energy, that is, atomic collapse. However, in the context of quantum mechanic, the atoms are stable in a Coulomb field due to the uncertainty principle. Indeed, the Coulomb potential created by the nucleus with a charge of Ze scales with $-Ze/r$, where r is the distance from the center of the nuclear charge, and the kinetic energy of the electron is given by $p^2/2m_e$. If the electron is restricted to a region of the space, its momentum uncertainty can be written as $p \sim h/r$, and the kinetic energy takes the form of $\sim h^2/2mr^2$. r must approach to zero in order to fall an electron to the nucleus. While the distance converges on zero, the kinetic energy of electron diverges more quickly than the potential energy, $-Ze/r$. As a result,

the situation is expected to be energetically forbidden.

This explanation brings up a new question related to the behaviour of a potential, scales with $-k/r^n$ where n $\geq$ 2, and which is more singular than the Coulomb potential. When the Schrödinger equation is solved in the presence of a potential scales with $-k/r^n$ in which a non-relativistic atomic collapse occurs. Quantum mechanical example of the fall-to-center problem has a bound energy solution when the strength k is larger than $h^2/(8me)$. If we take into account the relativistic effects, the Dirac equation has to be used instead of the Schrödinger equation, especially for superheavy atoms. It is well-known that the kinetic energy term in the Dirac equation is a linear function of momentum, that is $\sim h/r$, as expressed above. Indeed, the Coulomb potential in the Dirac equation also causes to atomic collapse.
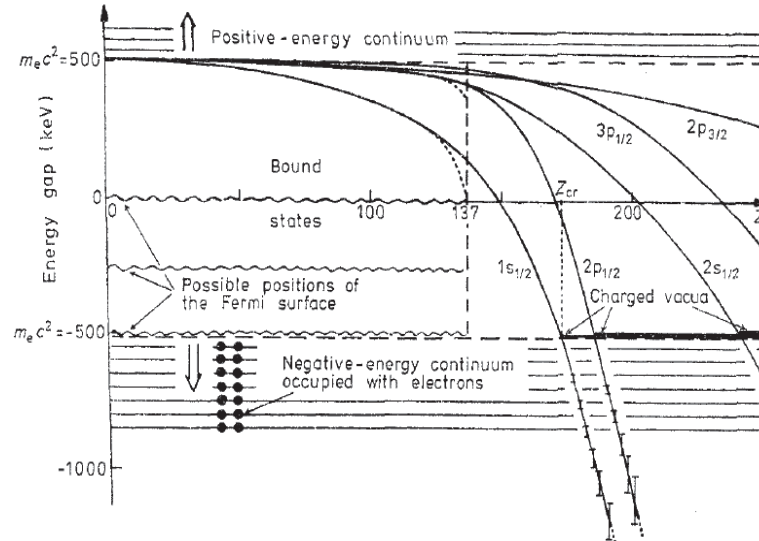
Figure 1.4. Energy spectrum of hydrogen atom for different Z values. Subcritical (Z < Z_c) and supercritical (Z > Z_c) regimes are separated by a critical valance charge of Z_c. A bound state turns out a resonance state in the negative energy continuum (Source: (Reinhardt and Greiner (1977)).

The exact solution of a three-dimensional Dirac equation in an external Coulomb field, produced by a point nucleus, is only consistent up to a critical threshold $Z_c = \alpha^{-1}$ $\sim$ 137, where $\alpha = e^2/\hbar c$ is the Sommerfeld fine-structure constant (Zeldovich and Popov (1972)). For larger values of the nuclear charge Z, the energy eigenvalues become purely imaginary, the wave function is non-normalizable, and its real part exhibits oscillatory behavior (Greiner (2000)). It was previously believed that such an equation could not

be solved. On the other had, the singularity of the point nucleus at the center leads to a non-self-adjoint Hamiltonian that could not be properly solved unless a finite-size for the nucleus is introduced (Pomeranchuk and Smorodinsky (1945)). This regularization results in a larger critical threshold of $Z_c \sim 172$ above which the wave function becomes a narrow resonance with a finite lifetime in compliance with Fano's formalism. The behaviour of atomic collapse states as a function of nuclear charge Z for the real atoms is shown in Fig.1.4 (Reinhardt and Greiner (1977)).

The lowest bound state $1S_{1/2}$ with the total angular momentum quantum number $j = 1/2$ dives into the negative energy continuum, and formerly bound state becomes a resonant state. In spite of its long-standing history (Greiner (2000)), such a phenomenon so-called collapse of the vacuum is far from being proven in experiments performed with real atoms (Schweppe et al. (1983); Cowan et al. (1985)). However, in terms of experimental accessibly, the situation is completely different in the single-layer graphene. Experimentally accessible Coulomb impurities are at the edge of supercritical regime, and putting them together, one can show the atomic collapse resonances in graphene, and as we will obtain with the help of numerical calculations, the same measurement and observation can be also possible in the finite sized graphene samples.

1.3. Coulomb Impurity Problem in Graphene

In the graphene version of atomic collapse, Dirac fermions form the vacuum itself, and the Coulomb impurity acts as a nucleus that couples to the vacuum by means of a dimensionless coupling strength $\beta = Z\alpha_g$, where $\alpha_g = 2.2/\kappa$ is the fine structure constant, Z is the nuclear charge of the impurity, and κ is the dielectric constant (Neto et al. (2009)). When β exceeds a critical coupling constant β_c, the lowest energy electron state of graphene firstly turns into a QBS (Pereira et al. (2007)), which corresponds to the $1S_{1/2}$ state of the impurity, and an infinite number of QBS can appear for massless Dirac fermions, depending on the value of β (Shytov et al. (2007a)). This critical value is estimated to be $\beta_c = 1/2$ in the case of non-interacting massless Dirac fermions (Khalilov and Ho (1998)), and graphene reduces the critical threshold for the the $1S_{1/2}$ state to $Z_c \gtrsim 1$ through a larger fine structure constant α_g (Pereira et al. (2007); Shytov et al. (2007a,b)). As for the size of the vacuum, the critical coupling constant remains the

same, i.e., $\beta_c = 1/2$ for the lowest angular momentum channel, when non-interacting Dirac fermions are confined in smaller-sized GQDs (Van Pottelberge et al. (2017)). But on the other hand, the role of electron interactions in this phenomenon seems to be important. A further extension of the problem takes electron interactions into account in which overscreening of the Coulomb impurity is reduced by electron-electron interactions, and this causes to increase in the critical threshold, which becomes slightly greater than a unit charge, .i.e., $Z_c > 1$ (Biswas et al. (2007); Terekhov et al. (2008)). The common point of these theoretical studies is that atomic collapse can be observed in graphene with the help of experimentally accessible Coulomb impurities such as calcium (Ca) dimers and cobalt (Co) trimmers (Wang et al. (2012, 2013)). Therefore, the idea of creating an artificial supercritical atom with a smaller critical valence charge has received considerable experimental attention (Wang et al. (2012, 2013); Mao et al. (2016); Wong et al. (2017); Lu et al. (2019)). Indeed, the formation of an infinite family of quasi-bound states in the presence of the clusters of charged Ca dimers on bulk graphene have been successfully monitored via the local density of states (LDOS) in an experimental study (Wang et al. (2013)).

On the other hand, all theoretical calculations have assumed a disorder-free graphene by ignoring the experimental facts (Hashimoto et al. (2004); Martin et al. (2008)), and the question of effects of imperfections on atomic collapse in graphene has not been addressed yet. Atomic scale defects (Meyer et al. (2008); Banhart et al. (2011)) and the intercalation of hydrogen atoms (McCreary et al. (2012); Wang et al. (2018); Çakmak et al. (2018)) may arise during the growth process, and these defects lead to an imperfect honeycomb lattice (Eckmann et al. (2012); Li et al. (2019)). Furthermore, such a deformed vacuum can fluctuate in response to spatial charge inhomogeneities caused by substrate (Burson et al. (2013); Özdemir et al. (2016)). To find out ambiguous consequences of these distortions beyond conventional perspective of the theory, the hexagonal GQDs with armchair edges (Güçlü et al. (2010)) could provide a practical playground, since these GQDs serve as a bridge between the finite-sized samples and bulk graphene thanks to their special band-gap characteristics (Güçlü et al. (2010, 2014)). Free of localized edge states, the band gap is proportional to the inverse square root of number of atoms ($E_{gap} \propto k_{min} \approx 2\pi/\Delta x \propto 1/\sqrt{N}$) (Sheng et al. (2012)). It corresponds to linear photon dispersion relation for confined Dirac fermions (Güçlü et al. (2010)). As

we will show in this thesis, atomic collapse can be observed in all sizes of these GQDs.

As for the vacuum polarization, the Coulomb impurity is screened by Dirac fermions leading to an effective charge of the impurity. It is calculated from the exact solution of 2D Dirac-Kepler problem for the subcritical and supercritical Coulomb potential in Ref. (Shytov et al. (2007b)). It can be noted that when the impurity has a subcritical charge, 2D Dirac-Kepler problem is consistent. For the supercritical charge, however, Dirac operator is not self-adjoint, and a finite size of the nucleus must be introduced, as previously explained. In addition, Dirac vacuum polarization changes its character in the supercritical regime. The study states that the polarization charge does not show long-range tail, and this charge is concentrated on the scale of Coulomb impurity radius in the subcritical regime. In the supercritical regime for non-interacting fermions, on the other hand, polarization charge scales with a power law form ($\sim 1/r^2$). This tail is due to additional term found in the scattering phase for the supercritical charge, and this additional term does not contribute to the polarization charge. Moreover, they show that there is an oscillation behaviour in the LDOS. Deviation from linear screening for supercritical impurities found in Ref. (Shytov et al. (2007b)) can be considered as an interesting example of the nonlinear screening.

In this thesis, starting from the pristine hexagonal GQDs with armchair edges, we construct a set of Dirac vacuums that differ in size, and we study electronic and transport properties of these vacuums with the help of the TB and the extended mean-field Hubbard (MFH) models in the presence of the central Coulomb impurity. The effects of the size of vacuum and electron-electron interactions on the critical coupling constant are investigated in greater detail. As previously mentioned, the size of the vacuum for both models does not cause any change in the critical value of the coupling strength, but the electron-electron interactions cause an increase in the critical threshold from $\beta_c = 0.5$ (TB) to $\beta_c = 0.6$ (MFH). In addition, the spin and valley symmetries are discussed, and spin-independent Coulomb impurity has no effect on the these symmetries for the clean vacuums. We also discuss the screening of the Coulomb impurity in different sized pristine hexagonal GQDs, and we calculate the effective charge of the impurity with the help of induced charge calculations. Furthermore, to reveal the role of vacuum imperfections, the critical threshold is studied by placing the Coulomb impurity at the center of disordered hexagonal GQDs. Deviations from the perfection in the vacuum

are intentionally created by: (1) randomly distributed point vacancies with different concentrations and (2) electron-hole puddles induced by Gaussian impurities. We find a strong dependence of the critical threshold on both types of disorder, leading to increase in the critical coupling constant. Some of these results have readily reported in our previous papers (Polat et al. (2020); Polat and Güçlü (2020)).

1.4. Single Charged Vacancy

Mao et al. (Mao et al. (2016)) demonstrated that a positive charge can be deposited into a single carbon vacancy by applying voltage pulses of $2 - 3$ V for > 10 seconds with the help of a scanning tunneling microscope (STM) tip. A charged vacancy in graphene is in analogy with the piling up positively charged ions and similarly leads to the sudden appearance of a sequence of QBS (Mao et al. (2016)). Besides, it is well-known that the removal of a single carbon atom lifts the spin and valley degrees of freedom (Neto et al. (2009)), hence the local magnetic moment is induced (Yazyev and Helm (2007)). Since only a prominent resonant peak is observed in previous studies (Ugeda et al. (2010, 2011)), the spin splitting has recently attracted attention in experiments (Zhang et al. (2016); González-Herrero et al. (2016)). In addition, for a while there has been significant progress in measurement of the valley splittings around a bare carbon vacancy (Li et al. (2019)) thanks to discrete energy levels and an unconventional method of preparation of GQDs (Freitag et al. (2016, 2018)). The question arises as to what sort of changes in physical properties happen after a bare vacancy is positively charged with the subcritical ($\beta > \beta_c$) and supercritical ($\beta < \beta_c$) Coulomb potentials.

In this sense, the hexagonal GQDS with armchair edges are advantageous. Of all the GQDs that have been reported so far (Ezawa (2007); Fernández-Rossier and Palacios (2007); Akola et al. (2008); Schnez et al. (2008); Mueller et al. (2010); Wimmer et al. (2010); Zarenia et al. (2011); Hämäläinen et al. (2011); Olle et al. (2012); Sheng et al. (2012); Subramaniam et al. (2012); Güçlü et al. (2014)), the hexagonal GQDs with armchair edges deserve attention due to well-known properties, among which, (1) sublattice symmetry results in spin symmetry; (2) two doubly degenerate levels in the vicinity of the FL account for the valley symmetry (Güçlü et al. (2014)). These internal properties indicate that the pristine hexagonal GQDs with armchair edges carry all the

four-fold symmetries of bulk graphene. Therefore, it becomes possible to follow the evolution of the spin and valley splittings as a function of the coupling strength β when a bare point vacancy is deliberately created, and its charge is gradually increased.

Here, the different sized hexagonal (triangular) GQDs with armchair (zigzag) edges are studied by using the TB and MFH models in the presence of a bare and a charged vacancy placed near the center (at the center) of the QD. Hubbard descriptions including electron-electron interactions and spin effects are investigated for not only a bare vacancy but also for a charged vacancy. The critical coupling constant is numerically found as $\beta_c \simeq 0.5$ and $\beta_c = 0.7$ for the non-interacting (TB) and the interacting (MFH) fermions, respectively. In addition, the valley splitting as a function of β is also studied. We found for the hexagonal GQDs that the spin splitting vanishes in the subcritical regime, but the valley splitting continues to exist in both regimes.

Furthermore, a charged Coulomb vacancy is placed at the center of triangular GQDs with zigzag edges. The effect of the charged vacancy on the electronic and magnetic properties has been analyzed in the absence of the spatial charge inhomogeneities. From a bare vacancy to a charged vacancy, the spin splitting has been extracted by LDOS calculations in the energy spectrum, which is significantly dominated by the edge states around the FL for the triangular GQDs. By approaching the vacancy, we obtained the spin splitting in such a complex energy spectrum, and the evolution of the spin splitting as a function of the coupling strength has been numerically examined.

Up to now, we introduce bulk graphene and the GQDs in Sec. 1.1, atomic collapse in QED in Sec. 1.2, the Coulomb impurity problem in graphene in Sec. 1.3, and a charged vacancy problem in Sec. 1.4. In particular, the Coulomb impurity problem starting from its original version to the current graphene version is introduced. Also, we have defined this phenomenon in the GQDs with some results from our previous articles published within the scope of this thesis (Polat et al. (2020); Polat and Güçlü (2020)). On the other hand, in the next chapter, the numerical methods employed thought this thesis will be introduced. We exactly solve the finite sized Hamiltonians within the TB and the MFH models, and in this way, we study the effect of charged impurities on the electronic, magnetic, and transport properties of the different sized hexagonal and triangular GQDs.

CHAPTER 2

THEORETICAL MODELS

This chapter contains our numerical methods such as the tight binding model, the extended Hubbard model within the mean field approximation, the details of the screening calculations, local density of states calculations, transport calculations, and the spin density calculations. By using these calculations, we successfully study different kinds of charged impurity problems in the GQDs.

The rest of this chapter is organized as follows. In Sec. 2.1, the tight binding model is discussed in greater detail from the bulk graphene to the finite sized samples. Sec. 2.2 introduces the extended Hubbard model, and the mean field approach is theoretically applied to this model in Sec. 2.3. In Sec. 2.4, the effective charge calculation is discussed. Sec. 2.5, Sec. 2.6, and Sec. 2.7 describe the local density of state, transmission coefficient, and spin density calculations, respectively.

2.1. Tight-Binding Model

The honeycomb lattice of graphene is actually a combination of two triangular Bravais lattices, which are nonequivalent A and B sublattices, and the distances between these two sublattices is known as the carbon-carbon distance a = 1.42 Å. In this system, $\mathbf{a}_{1,2}$ = a/2$(\pm\sqrt{3}, 3)$ are the primitive unit vectors. The positions of all sublattices can be derived from these primitive vectors as follows:

$$\mathbf{R}_A = n\mathbf{a}_1 + m\mathbf{a}_2 + \mathbf{b}$$
$$\mathbf{R}_B = n\mathbf{a}_1 + m\mathbf{a}_2, \tag{2.1}$$

where n and m are integer numbers, and the vector $\mathbf{b}$ goes from the A (red) sublattice to the B (blue) sublattice in the unit cell, as shown in Fig. 2.1. In this thesis, we model the non-interacting fermions with the help of TB approach, whereas we will use the mean field Hubbard model to describe the π_z dynamics of the interacting fermions. The latter will be introduced in the next section. As for the lattice, two dimensional honeycomb

lattice can be constructed via these primitive vectors for A and B sublattices. The single electron wave function on sublattice A can be expressed through a linear combination of the π_z orbitals of the A sublattices, whereas the single electron wave function on sublattice B can be expressed through a linear combination of the π_z orbitals of the B sublattices as follows:

$$\Psi_{\mathbf{k}}^{\mathbf{A}}(\mathbf{r}) = \frac{1}{\sqrt{N_U}} \sum_{\mathbf{R_A}} e^{i\mathbf{k}\mathbf{R_A}} \Phi_z(\mathbf{r} - \mathbf{R_A})$$

$$\Psi_{\mathbf{k}}^{\mathbf{B}}(\mathbf{r}) = \frac{1}{\sqrt{N_U}} \sum_{\mathbf{R_B}} e^{i\mathbf{k}\mathbf{R_B}} \Phi_z(\mathbf{r} - \mathbf{R_B}). \qquad (2.2)$$

Here, the wave vector $\mathbf{k}$ labels the wave functions owing to the transition symmetry and Bloch's theorem, $\sqrt{N_U}$ stands for the number of unit cells, $\Phi_z(\mathbf{r} - \mathbf{R_{A,B}})$ represents the orthogonal π_z orbitals at the position $\mathbf{R}$, and the expansion coefficients can be expressed by the terms $e^{i\mathbf{k}\mathbf{R_{A,B}}}$.
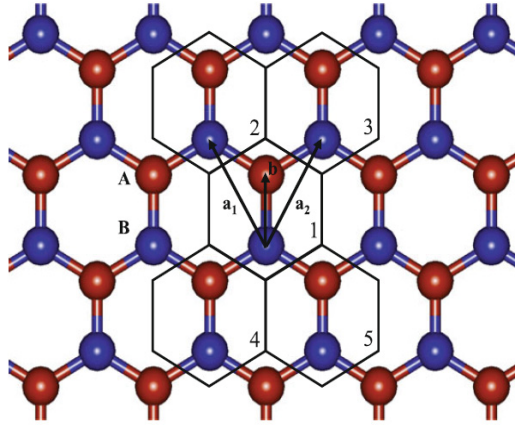
Figure 2.1. Graphene honeycomb lattice with A (red) and B (blue) atoms in a unit cell. Here, **b** defines a vector between these two atoms in the unit cell (Source: (Güçlü et al. (2014)).

One can extract the wave functions by using above equations. Starting from these equations, the total electron wave function can be written as follows:

$$\Psi_{\mathbf{k}}(\mathbf{r}) = A_{\mathbf{k}} \Psi_{\mathbf{k}}^{\mathbf{A}}(\mathbf{r}) + B_{\mathbf{k}} \Psi_{\mathbf{k}}^{\mathbf{B}}(\mathbf{r}), \qquad (2.3)$$

where the coefficients A_k and B_k can be found with the help of the diagonalization of the Hamiltonian matrix, and $\Psi_{\mathbf{k}}^{\mathbf{A}}(\mathbf{r})$ and $\Psi_{\mathbf{k}}^{\mathbf{B}}(\mathbf{r})$ are the orthogonal wave functions. These wave functions can be written into the tight-binding Hamiltonian to calculate the energy

dispersion relation of the unit cell. In this way, the π_z dynamics of the non-interacting Dirac fermions can be studied. The tight-binding Hamiltonian is given by

$$H(\mathbf{k}) = \begin{pmatrix} \langle \boldsymbol{\Psi}_{\mathbf{k}}^{\mathbf{A}} | H | \boldsymbol{\Psi}_{\mathbf{k}}^{\mathbf{A}} \rangle & \langle \boldsymbol{\Psi}_{\mathbf{k}}^{\mathbf{A}} | H | \boldsymbol{\Psi}_{\mathbf{k}}^{\mathbf{B}} \rangle \\ \langle \boldsymbol{\Psi}_{\mathbf{k}}^{\mathbf{B}} | H | \boldsymbol{\Psi}_{\mathbf{k}}^{\mathbf{A}} \rangle & \langle \boldsymbol{\Psi}_{\mathbf{k}}^{\mathbf{B}} | H | \boldsymbol{\Psi}_{\mathbf{k}}^{\mathbf{B}} \rangle \end{pmatrix} \tag{2.4}$$

in which $\boldsymbol{\Psi}_{\mathbf{k}}^{\mathbf{A}}(\mathbf{r})$ and $\boldsymbol{\Psi}_{\mathbf{k}}^{\mathbf{B}}(\mathbf{r})$ are the orthogonal wave functions, as previously mentioned, and Hamiltonian is given by H = $p^2/2m + \sum_{\mathbf{R_A}} V(\mathbf{r} - \mathbf{R_A}) + \sum_{\mathbf{R_B}} V(\mathbf{r} - \mathbf{R_B})$. Terms $\langle \boldsymbol{\Psi}_{\mathbf{k}}^{\mathbf{A}} | H | \boldsymbol{\Psi}_{\mathbf{k}}^{\mathbf{A}} \rangle$ and $\langle \boldsymbol{\Psi}_{\mathbf{k}}^{\mathbf{B}} | H | \boldsymbol{\Psi}_{\mathbf{k}}^{\mathbf{B}} \rangle$ are assumed to be zero within the nearest neighbours approximation, whereas the cross terms can be explicitly written as follows:

$$\langle \boldsymbol{\Psi}_{\mathbf{k}}^{\mathbf{B}} | H | \boldsymbol{\Psi}_{\mathbf{k}}^{\mathbf{A}} \rangle = \frac{1}{N_U} \sum_{\langle \mathbf{R_A}, \mathbf{R_B} \rangle} e^{i\mathbf{k}(\mathbf{R_A} - \mathbf{R_B})} \int d\mathbf{r} \Phi_z^*(\mathbf{r} - \mathbf{R_B}) V(r - \mathbf{R_B}) \Phi_z(\mathbf{r} - \mathbf{R_A})$$

$$\langle \boldsymbol{\Psi}_{\mathbf{k}}^{\mathbf{A}} | H | \boldsymbol{\Psi}_{\mathbf{k}}^{\mathbf{B}} \rangle = \frac{1}{N_U} \sum_{\langle \mathbf{R_A}, \mathbf{R_B} \rangle} e^{i\mathbf{k}(\mathbf{R_A} - \mathbf{R_B})} \underbrace{\int d\mathbf{r} \Phi_z^*(\mathbf{r} - \mathbf{R_A}) V(r - \mathbf{R_A}) \Phi_z(\mathbf{r} - \mathbf{R_B})}_{\text{the hopping integral } t}$$

$$\tag{2.5}$$

in which we restrict ourselves only to the nearest neighbours. The hopping integral is $t = \int d\mathbf{r} \Phi_z^*(\mathbf{r} - \mathbf{R_A}) V(r - \mathbf{R_A}) \Phi_z(\mathbf{r} - \mathbf{R_B})$ = -2.8 eV (Neto et al. (2009)). The above equation will become

$$\langle \boldsymbol{\Psi}_{\mathbf{k}}^{\mathbf{A}} | H | \boldsymbol{\Psi}_{\mathbf{k}}^{\mathbf{B}} \rangle = t(e^{-i\mathbf{kb}} + e^{-i\mathbf{k}(\mathbf{b}-\mathbf{a_1})} + e^{-i\mathbf{k}(\mathbf{b}-\mathbf{a_2})})$$

$$\langle \boldsymbol{\Psi}_{\mathbf{k}}^{\mathbf{B}} | H | \boldsymbol{\Psi}_{\mathbf{k}}^{\mathbf{A}} \rangle = t(e^{i\mathbf{kb}} + e^{i\mathbf{k}(\mathbf{b}-\mathbf{a_1})} + e^{i\mathbf{k}(\mathbf{b}-\mathbf{a_2})}). \tag{2.6}$$

Finally, we define $f(\mathbf{k}) = (e^{-i\mathbf{kb}} + e^{-i\mathbf{k}(\mathbf{b}-\mathbf{a_1})} + e^{-i\mathbf{k}(\mathbf{b}-\mathbf{a_2})})$, and we can write

$$E_{\pm}(\mathbf{k}) = \pm t f(\mathbf{k}), \tag{2.7}$$

which corresponds to the band structure of graphene. The conduction and valance bands meet at the six corners of the Brillouin zone, which indicates that graphene has zero band gap at the K and K' points of the first Brillouin zone.

In finite sized samples, we study the TB model by exactly diagonalize the NxN matrix in which N is the number of carbon atoms. As given below in Eq. 2.8, in our numerical calculations, we only take into account the nearest neighbour hopping of the electrons, and the hopping term is taken to be t = -2.8 eV (Neto et al. (2009)). In addition, the on-site energies of π_z orbitals can be taken to be zero leading to the other terms in the matrix is zero. In this manner, the tight-binding Hamiltonian will be the backbone of

15

our extended mean-field Hubbard calculations. The tight binding matrix can be written as follows:

$$H_{TB} = \begin{pmatrix} 0 & t & \dots & t \\ t & 0 & \dots & 0 \\ \vdots & \vdots & \ddots & \vdots \\ t & 0 & \dots & 0 \end{pmatrix}_{N \times N} . \tag{2.8}$$

Here, this matrix has been written by assuming that the atom indexed as i = 1 and the atom indexed as j = 2 are the nearest neighbour to each other. The same assumption is also done for the atoms indexed as i = 1 and j = N. The term t is used for the hopping of the electron from the atomic site of i = 1 to atomic site of j = 2. The same hopping parameter has to be written in the Hamiltonian for hopping from the atomic site of i =2 to i = 1. Next, we will give the details how we add the onsite and the offsite Coulomb repulsion terms to such a matrix.

2.2. Extended Hubbard Model

One can start with the many-body Hamiltonian in second quantized form, and such a Hamiltonian can be expressed in terms of creation and annihilation operators as follows:

$$H = \sum_{pq} \hat{t}_{pq} c_p^\dagger c_q + \frac{1}{2} \sum_{qprs} \left\langle pq | \hat{V} | rs \right\rangle c_p^\dagger c_q^\dagger c_r c_s \tag{2.9}$$

in which the terms $\hat{t}$ and $\hat{V}$ are independent of the spin. On the other hand, the terms p, q, r, and s depend on the spin, and these terms can be represented by the following states, which are $p = i\sigma$, $q = j\sigma'$, $r = k\sigma''$, and $s = l\sigma'''$, respectively. When these four terms with spin dependency are rewritten into Eq. 2.9, the first term on the right hand side can be written as follows:

$$\hat{t}_{pq} = \langle p|t|q \rangle = \left\langle i\sigma|t|j\sigma' \right\rangle = \langle i|t|j \rangle \left\langle \sigma|\sigma' \right\rangle = t_{ij}\delta_{\sigma\sigma'}, \tag{2.10}$$

and the second term on the right hand side has to be expanded under these assumptions. This interaction term will be divided into two main interactions, which are onsite and offsite Coulomb repulsions. In this manner, it can be rewritten with the help of spin

dependency of the above four terms as follows:

$$\hat{V}_{pqrs} = \left\langle pq|\hat{V}|rs\right\rangle = \left\langle i\sigma\right| \left[\left\langle j\sigma'|\hat{V}|k\sigma''\right\rangle\right] l\sigma'''\right\rangle$$

$$= \left\langle i\right| \left[\left\langle j|\hat{V}|k\right\rangle\right] |l\right\rangle \left\langle \sigma\right| \left[\left\langle \sigma'|\sigma''\right\rangle\right] |\sigma'''\right\rangle = \hat{V}_{ijkl}\delta_{\sigma'\sigma''}\delta_{\sigma\sigma'''}. \quad (2.11)$$

When Eq. 2.10 and Eq. 2.11 are rewritten into Eq. 2.9, the non-zero values have to be held. After that, the many-body Hamiltonian becomes

$$H = \sum_{\langle ij\sigma\rangle} \hat{t}_{ij}c_{i\sigma}^{\dagger}c_{j\sigma} + \frac{1}{2} \sum_{ijkl\sigma\sigma'} \left\langle ij|\hat{V}|kl\right\rangle c_{i\sigma}^{\dagger}c_{j\sigma'}^{\dagger}c_{k\sigma'}c_{l\sigma}, \quad (2.12)$$

where the Coulomb matrix elements in the integral form are given by

$$\left\langle ij|\hat{V}|kl\right\rangle = \int\int d\mathbf{r}_1 d\mathbf{r}_2 \psi_i^*(\mathbf{r}_1)\psi_j^*(\mathbf{r}_2)\frac{2}{\kappa|\mathbf{r}_2 - \mathbf{r}_1|}\psi_k(\mathbf{r}_2)\psi_l(\mathbf{r}_1). \quad (2.13)$$

Here, $\mathbf{r}_1$ and $\mathbf{r}_2$ are the position of first and second electrons, respectively. If the equations $l = i$ and $k = j$ are satisfied, $\left\langle ij|\hat{V}|kl\right\rangle$ becomes $\left\langle ij|\hat{V}|ji\right\rangle$, which is the Coulomb interaction between two electrons in the lattice sites i and j. As an another option, $\left\langle ij|\hat{V}|kl\right\rangle$ is equivalent to the exchange term $\left\langle ij|\hat{V}|ij\right\rangle$ if $l = j$ and $k = i$. The exchange term is only possible for electrons on the lattice sites i and j with the same spin $\sigma = \sigma'$.

We restrict ourselves in order to obtain the exchange term, which is in compliance with the Pauli-exclusion principle. It dictates that the spin components have to be different from each other $\sigma \neq \sigma'$. In this approach, we can assume the following equality between our four indexes as $i = j = k = l$. Starting from this fact, the last expression in Eq. 2.12 turns into the exchange term with the help of $\left\langle ij|\hat{V}|kl\right\rangle = \left\langle ii|\hat{V}|ii\right\rangle = \text{U}$. It can be expressed as

$$\frac{1}{2} \sum_{ijkl\sigma\sigma'} \left\langle ij|\hat{V}|kl\right\rangle c_{i\sigma}^{\dagger}c_{j\sigma'}^{\dagger}c_{k\sigma'}c_{l\sigma} = \frac{1}{2}U \sum_{i,\sigma\neq\sigma'} c_{i\sigma}^{\dagger}c_{i\sigma'}^{\dagger}c_{i\sigma'}c_{i\sigma}. \quad (2.14)$$

With the help of the communication relations: (1) $\{c_{i\sigma'}, c_{i\sigma}\} = 0$ for $\sigma \neq \sigma' \rightarrow c_{i\sigma'}c_{i\sigma} = -c_{i\sigma}c_{i\sigma'}$ and (2) $\{c_{i\sigma'}^{\dagger}, c_{i\sigma}\} = 0 \rightarrow c_{i\sigma'}^{\dagger}c_{i\sigma} = -c_{i\sigma}c_{i\sigma'}^{\dagger}$, and by introducing the number operator as $n_{i\sigma} = c_{i\sigma}^{\dagger}c_{i\sigma}$, Eq. 2.14 reads

$$\frac{1}{2}U \sum_{i,\sigma\neq\sigma'} c_{i\sigma}^{\dagger}c_{i\sigma'}^{\dagger}c_{i\sigma'}c_{i\sigma} = \frac{1}{2}U \sum_{i\sigma\sigma'} n_{i\sigma}n_{i\sigma'} = U \sum_{i} n_{i\uparrow}n_{i\downarrow}, \quad (2.15)$$

where the factor of 1/2 is cancelled by two exchange terms. As for the Coulomb interaction, the equations $l = i$ and $k = j$ lead to an another expression as $\left\langle ij|\hat{V}|kl\right\rangle$

17

$= \left\langle ij|\hat{V}|ji \right\rangle = \hat{V}_{ij}$. For the last term in Eq. 2.12, the communication relations of (1) $\{c_{j\sigma'}, c_{i\sigma}\} = 0 \rightarrow c_{j\sigma'}c_{i\sigma} = -c_{i\sigma}c_{j\sigma'}$ and (2) $\{c_{j\sigma'}^{\dagger}, c_{i\sigma}\} = 0 \rightarrow c_{j\sigma'}^{\dagger}c_{i\sigma} = -c_{i\sigma}c_{j\sigma'}^{\dagger}$ can be used. The resulting equation is

$$\frac{1}{2}\sum_{ijkl\sigma\sigma'}\left\langle ij|\hat{V}|kl \right\rangle c_{i\sigma}^{\dagger}c_{j\sigma'}^{\dagger}c_{k\sigma'}c_{l\sigma} = \frac{1}{2}\sum_{ij\sigma\sigma'}\hat{V}_{ij}c_{i\sigma}^{\dagger}c_{j\sigma'}^{\dagger}c_{j\sigma'}c_{i\sigma} = \frac{1}{2}\sum_{ij\sigma\sigma'}\hat{V}_{ij}n_in_j. \quad (2.16)$$

To obtain the final form of the many-body Hamiltonian including the exchange and the Coulomb interactions, Eq. 2.15 and Eq. 2.16 have to added to each other. The final form of Hamiltonian in Eq. 2.9 is given as follows:

$$H = \underbrace{\underbrace{\sum_{\langle ij\sigma\rangle}\hat{t}_{ij}c_{i\sigma}^{\dagger}c_{j\sigma} + U\sum_{i}n_{i\uparrow}n_{i\downarrow}}_{\text{Hubbard Model}} +\frac{1}{2}\sum_{ij\sigma\sigma'}\hat{V}_{ij}n_in_i}_{\text{Extended Hubbard Model}}\,. \quad (2.17)$$

The first two terms refer to the Hubbard Hamiltonian, whereas all terms are known as the extended Hubbard Hamiltonian. Since this Hamiltonian can not be solved for a system consisting of many electrons, we have to employ the mean-field approach. In this assumption, an electron moves in a mean field, which is created by other electrons in the system.

2.3. Mean Field Approach

In this section, we will study a mean-field approach for the extended Hubbard model. To employ the mean-field approach, which assumes an electron moving in a field created by other electrons in the system, we will make assumptions with the expansions. In this approach, Δn terms are assumed to be negligibly small within the mean field approach. In this manner, we can expand the terms $n_{i\uparrow}$ and $n_{i\downarrow}$ in Eq. 2.17 in terms of Δn terms as follows:

$$n_{i\uparrow} = \langle n_{i\uparrow}\rangle + \underbrace{(n_{i\uparrow} - \langle n_{i\uparrow}\rangle)}_{\Delta n_{i\uparrow}}$$

$$n_{i\downarrow} = \langle n_{i\downarrow}\rangle + \underbrace{(n_{i\downarrow} - \langle n_{i\downarrow}\rangle)}_{\Delta n_{i\downarrow}}\,. \quad (2.18)$$

When these expressions are written instead of $n_{i\uparrow}n_{i\downarrow}$ and n_in_j products, the following equations can be obtained: (1) $n_{i\uparrow}n_{i\downarrow} = n_{i\uparrow}\langle n_{i\downarrow}\rangle + n_{i\downarrow}\langle n_{i\uparrow}\rangle + \langle n_{i\uparrow}\rangle\langle n_{i\downarrow}\rangle$, and the other one

(2) $n_i n_j = n_i \langle n_j \rangle + n_j \langle n_i \rangle + \langle n_i \rangle \langle n_j \rangle$, respectively. Thus, the many-body Hamiltonian is written by putting these terms instead of the Hubbard interaction terms as follows:

$$H \approx H_{MF} = \sum_{\langle ij\sigma \rangle} \hat{t}_{ij} c_{i\sigma}^\dagger c_{j\sigma} + U(n_{i\uparrow} \langle n_{i\downarrow} \rangle + n_{i\downarrow} \langle n_{i\uparrow} \rangle + \langle n_{i\uparrow} \rangle \langle n_{i\downarrow} \rangle)$$

$$+ \frac{1}{2} \sum_{ij\sigma\sigma'} \hat{V}_{ij}(n_i \langle n_j \rangle + n_j \langle n_i \rangle + \langle n_i \rangle \langle n_j \rangle). \qquad (2.19)$$

Such an equation is actually quadratic in terms of $c_{i\sigma}^\dagger c_{j\sigma}$, which can be accepted as follows:

$$H_{MF} \to H_{MF}^{BULK} = \sum_{ij\sigma} \hat{\tau}_{ij} c_{i\sigma}^\dagger c_{j\sigma}, \qquad (2.20)$$

and the following assumptions can be made for a bulk structure to produce results related to half-filled model, which are given as follows:

$$\langle n_i \rangle = 1$$
$$\langle n_{i\sigma} \rangle = \frac{1}{2}. \qquad (2.21)$$

As a result, we can write the following equation under these assumptions

$$H_{MF} = H_{MF} - H_{MF}^{BULK} + H_{MF}^{BULK}$$

$$= \sum_{\langle ij\sigma \rangle} \hat{t}_{ij} c_{i\sigma}^\dagger c_{j\sigma} + U \sum_i n_{i\uparrow} n_{i\downarrow} + \frac{1}{2} \sum_{ij\sigma\sigma'} \hat{V}_{ij} n_i n_j$$

$$- \sum_{\langle ij\sigma \rangle} \hat{t}_{ij} c_{i\sigma}^\dagger c_{j\sigma} - \frac{U}{2} \sum_i (n_{i\uparrow} + n_{i\downarrow} - \frac{1}{2}) + -\frac{1}{2} \sum_{ij\sigma\sigma'} \hat{V}_{ij}(n_i + n_j - 1)$$

$$+ \sum_{ij\sigma} \hat{\tau}_{ij} c_{i\sigma}^\dagger c_{j\sigma}, \qquad (2.22)$$

after the necessary arrangements are done, as well as, $\hat{V}_{ij} = \hat{V}_{ji}$ and $(\langle n_i \rangle - 1)n_j = (\langle n_j \rangle - 1)n_i$, this equation can be reduced to the extended mean-field Hubbard model. Its Hamiltonian reads

$$H_{MFH} = t \sum_{\langle ij \rangle \sigma} \left(c_{i\sigma}^\dagger c_{j\sigma} + \text{H.c.} \right) + U \sum_{i\sigma} \left(\langle n_{i\bar{\sigma}} \rangle - \frac{1}{2} \right) n_{i\sigma}$$

$$+ \sum_{ij} V_{ij} \left(\langle n_j \rangle - 1 \right) n_i, \qquad (2.23)$$

where the first term describes the tight-binding Hamiltonian with a hopping amplitude of t = -2.8 eV in which the operator $c_{i\sigma}^\dagger$ ($c_{i\sigma}$) creates (annihilates) an electron with spin σ at the

lattice site i. $U = 16.52/\kappa$ eV is the onsite Coulomb repulsion (Güçlü et al. (2014)), where $\kappa = 6$ is equivalent to that of the SiO$_2$ substrate under the effects of interband polarization (Ando (2006)). $\langle n_{i\sigma} \rangle$ is the spin-dependent expectation value of electron densities, and $n_{i\sigma}$ is the spin-dependent number operator. Third term V_{ij} is associated with the off-site Coulomb repulsion, which is set to be $8.64/\kappa$ eV, $5.33/\kappa$ eV, and $27.21/\kappa d_{ij}$ eV for the nearest-neighbors, next-nearest-neighbors, and the remote atomic sites, respectively (Güçlü et al. (2014); Potasz et al. (2010)). d_{ij} is the distance between the sites i and j at relatively large distances, and it is in atomic units. Since the last Hamiltonian excludes any quadratic terms in terms of $c_{j\sigma}$, the Hamiltonian has a quartic structure, presently. Notwithstanding, since we don't have the occupation numbers in the Hamiltonian, one can start with the initial matrices. In this manner, the TB Hamiltonian, with the n and m numbers in $\mathbf{R_B}$ and $\mathbf{R_B}$ vectors, one can obtain the complete Hamiltonian consisting of the electron-electron interactions by adding U and V_{ij} terms into the TB Hamiltonian.

For the Coulomb impurity problem, we solve the extended mean-field theory of the Hubbard model starting from a single-band tight-binding approximation for π_z orbitals. The π_z electron dynamics are described by the following effective Hamiltonian

$$
H_{MFH} = t \sum_{\langle ij \rangle \sigma} \left(c_{i\sigma}^{\dagger} c_{j\sigma} + \text{H.c.} \right) + U \sum_{i\sigma} \left(\langle n_{i\overline{\sigma}} \rangle - \frac{1}{2} \right) n_{i\sigma}
$$
$$
+ \sum_{ij} V_{ij} \left(\langle n_j \rangle - 1 \right) n_i - \hbar v_{\text{F}} \beta \sum_{i\sigma} \frac{c_{i\sigma}^{\dagger} c_{i\sigma}}{r_i}, \tag{2.24}
$$

Herein the nearest neighbor hopping term t preserves the electron-hole symmetry in the absence of the Coulomb potential (Pereira et al. (2007)). The second term is the on-site interaction term in which only two electrons with opposite spin can occupy the same lattice site by paying an extra correlation energy of U. The last term stands for the Coulomb potential in which r_i is the distance between the lattice site i and the center of the Coulomb potential (Moldovan and Peeters (2016)), and v_{F} is the Fermi velocity. The coupling constant β is assumed to be attractive (> 0) without loss of generality.

2.4. Screening Calculations

As the coupling strength β is increased, the charge in the vicinity of the central Coulomb potential is induced (Pereira et al. (2008)). Such an charge inducement reduces

the charge of the impurity, and this is known as the screening of the impurity, which can be written as $Z_{eff.} = Z_{bare} - Q_{ind.}$, where $Q_{ind.}$ is the induced background charge. In the subcritical regime, the total induced charge $Q_{ind.}$ can be obtained by integrating the charge density $\delta p(r)$, which can be written as follows:

$$\delta p(r) = \sum_{E<E_F} |\Psi(r)|^2 - \sum_{E<E_F} |\Psi^0(r)|^2, \tag{2.25}$$

where $\Psi(r)$ and $\Psi^0(r)$ are the discrete set of wave functions in the presence and absence of the Coulomb potential, respectively. However, the induced background charge vanishes if the polarization charge density $\delta p(r)$ is summed up over all atomic sites; therefore, a circle centered around the impurity with a finite radius R_{max} is needed (Shytov et al. (2007b); Kotov et al. (2008)). For this reason, the value of the induced charge Q(R) is maximized and will be expressed as Q_{max} inside a radius of R_{max}. Starting from the above equation, we compute the maximum induced charge Q_{max} within R_{max} as follows:

$$Q_{max}(r) = N \int_{R_{max}<R} \delta p(r) dr, \tag{2.26}$$

where N = 2 is the degeneracy of the problem (Pereira et al. (2008)), which is used for both the TB and extended mean field Hubbard models. Effective charge of the impurity for different sized clean GQDs is our quantity of interest, especially in the presence of electron-electron interactions in this thesis.

2.5. Local Density of State Calculations

Since the Coulomb potential inversely proportional to the distance, one can measure the strongest effect from the atoms closest to the potential. In this manner, LDOS measurement is important for such a potential (Shytov et al. (2007a)). LDOS is experimentally accessible through a STM (Wang et al. (2013)) and is calculated by

$$N(E,r) = \sum_i |\Psi_i(r)|^2 \delta(E - E_i), \tag{2.27}$$

where $\Psi(r)$ is the normalized wave function, the energy E is identical to applied bias voltage in STM measurements, and E_i is the eigenenergy of the ith state. The LDOS is the spatially resolved density of states (DOS), which is calculated by summing the

discrete energy levels of the GQDs at a set of radial distances from the impurity, ranging from r = 0.142 nm up to r = 1.136 nm. The summations are performed by using a Gaussian membership function with a standard deviation of σ = 0.2 eV in a linearly spaced energy interval $E \in$ [-2.5,2.5]. Since the effects of random disorders may differ from atom to atom, these calculations are separately carried out for each individual atom at the predefined radial distances, and this is repeated in ten random disorder distributions for each of the disordered configurations. Finally, the LDOS spectra per lattice site at various distances are extracted by averaging over these samples in this thesis.

2.6. Transmission Coefficients

In this section, we will introduce the transmission calculations of the GQDs in the presence of a central Coulomb impurity. The same method has been utilized in the subcritical regime and supercritical regime. We utilize the retarded Green's function in energy domain to calculate the transmission coefficients in the GQDs. As a minimum model for quantum transport calculations, Hamiltonian of the left-center-right (LRC) system reads

$$\begin{pmatrix} H_{LL} & H_{LC} & 0 \\ H_{CL} & H_{CC} & H_{CR} \\ 0 & H_{RC} & H_{RR} \end{pmatrix} \begin{pmatrix} \Psi_L \\ \Psi_C \\ \Psi_R \end{pmatrix} = E \begin{pmatrix} \Psi_L \\ \Psi_C \\ \Psi_R \end{pmatrix}, \tag{2.28}$$

where H_{LL} (H_{RR}) is Hamiltonian of the left (right) lead, and H_{CC} is the central Hamiltonian, which is of our interest. $H_{LC} = H_{CL}^\dagger$ and $H_{RC} = H_{CR}^\dagger$ refer to the coupling between the left lead and the central region and the coupling between the right lead and the central region, respectively. $\Psi_{L,C,R}$ is the wave function of the related region. By considering the retarded Green's function in energy domain as $G(E) = ((E+i0^+)I_{N \times N} - H)^{-1}$, where $0^+ = 10^{-6} \times t$ is an infinitesimal positive number in our calculations, one can write the following equation:

$$\begin{pmatrix} E - H_{LL} \pm i0^+ & -H_{LC} & 0 \\ -H_{CL} & E - H_{CC} \pm i0^+ & -H_{CR} \\ 0 & -H_{RC} & E - H_{RR} \pm i0^+ \end{pmatrix} \begin{pmatrix} G_{LL} & G_{LC} & G_{LR} \\ G_{CL} & G_{CC} & G_{CR} \\ G_{RL} & G_{RC} & G_{RR} \end{pmatrix} = 1. \tag{2.29}$$

By solving this equation as given elsewhere (Zhou (2017)), one can obtain

$$G(E) = ((E + i0^+)I_{N \times N} - H_c - \Sigma_L - \Sigma_R)^{-1}, \tag{2.30}$$

where $\Sigma_\alpha = H_{C\alpha}G^0_{\alpha\alpha}H_{\alpha C}$ is the self energy function of the probes. The wave function in the left lead can be written in terms of an transmitted wave Ψ^0_L and an reflected wave Ψ^1_L functions as follows: $\Psi_L = \Psi^0_L + \Psi^1_L$, which can be inserted into Eq. 2.28. With the help of Eq. 2.30 and the self energy function of the probes, the following equations can be written

$$\Psi_L = (1 + G^0_{LL}H_{LC}G_{CC}H_{CL})\Psi^0_L,$$
$$\Psi_C = G_{CC}H_{CL}G_{CC}\Psi^0_L, \tag{2.31}$$
$$\Psi_R = G^0_{RR}H_{RC}G_{CC}H_{CL}\Psi^0_L, \tag{2.32}$$

where $G^0_{\alpha\alpha}$ is the Green′s function of the isolated leads. We can obtain the current contribution of the left lead by using the probability current formula when the steady state current is established. Such a contribution from left lead to the central region reads

$$J_L = \frac{1}{\hbar}\Psi^{0\dagger}_L H_{LC}G^\dagger_{CC}\Gamma_R G_{CC}H_{CL}\Psi^0_L, \tag{2.33}$$

where $\Gamma_R = \Sigma_R - \Sigma^\dagger_R$. For a state Ψ^0_{kL} with quantum number k, the total probability current from the left lead to the central region can be found as follows:

$$I_L = \frac{1}{\hbar}\int_{-\infty}^{\infty} dE Tr(G^\dagger_{CC}\Gamma_R G_{CC}\Gamma_L)f_L(E). \tag{2.34}$$

Here, $f_L(E)$ is the Fermi function of the left lead, which is assumed to be the same for both leads. The total steady state probability current is the sum of left and right contributions as $I = I_L + I_R$, which reads

$$I = \frac{1}{\hbar}\int_{-\infty}^{\infty} dE T(E)|f_L(E) - f_R(E)|, \tag{2.35}$$

where the transmission coefficient $T(E)$ equals the following equation

$$T(E) = Tr(\Gamma^L(E)G(E)\Gamma^R(E)G^T(E)), \tag{2.36}$$

where generic electrodes are used in order to avoid structural features arising from the electrodes in the resulting transmission spectra. For that purpose, a one-dimensional wide bandwidth tight-binding chain is assumed. Self energies matrices ($\Sigma_{N \times N}$) for the right

and left leads are obtained from the analytical solution of surface Green function (Müller et al. (2000)).

The probes are placed at the ends of the hexagonal GQDs with armchair edges, and the hopping term from the leads to the central region is taken to be as t/4. To calculate transmission coefficients, the Coulomb impurity problem in the hexagonal GQDs with armchair edges is set, as shown in Fig. 2.2. Here, in the position of the left and right leads can be seen. By taking different size hexagonal GQDs with armchair edges, we study the effect of the Coulomb impurity on the transmission coefficients of the lowest bound state in the subcritical and the supercritical regimes. In Eq. 2.36, $\Gamma^{L,R}$'s are equivalent to
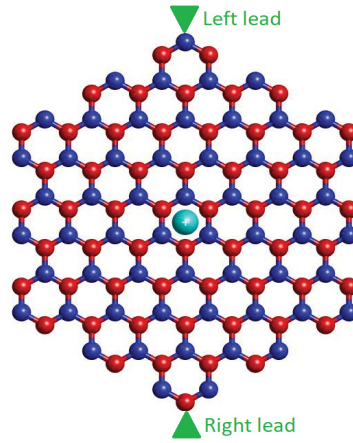
Figure 2.2. shows that the Coulomb potential is placed at the center of the hexagonal GQD. Here, the left and right leads are placed at the end of the same dot, but the size of this dot is gradually increased in our calculations.

the corresponding broadening matrices, and the hopping parameter of *t* in the reservoirs is taken into account (Müller et al. (2000)). The transmission coefficients around the resonance energies of the defect-induced and the lowest bound sates, i.e., atomic collapse states, are numerically calculated for different values of β. In this way, we study the effect of the coupling constant in the transport properties of th GQDs.

2.7. Spin Density Calculations

Spin density calculations is important not only in the presence of the edge states but also in the presence of a single bare or a charged vacancy to reveal the difference

between spin-up and spin-down fermions in the lattice sites. In the presence of a single charged vacancy, starting from the self-consistent expectation values of electron densities, we compute the spin density per lattice site as follows:

$$< s_i^z >= m_i = (< n_{i\uparrow} > - < n_{i\downarrow} >)/2, \qquad (2.37)$$

where $<n_{i\sigma}>$'s are calculated by summing up all states lying below Fermi level. Here, the total spin of the system is given by $S = \sum_i < s_i^z >$ (Yazyev (2010)). Starting from Eq. 2.37, the staggered magnetization as an order parameter of the antiferromagnetism is numerically calculated from

$$\mu_s^z = \sum_i (-1)^i < s_i^z >, \qquad (2.38)$$

where $(-1)^i$ indicates that the contributions are summed up from the opposite sublattices with opposite signs. Here μ_s^z is proportional to the antiferromagnetism of the structure (Grujić et al. (2013)).

In the next chapter, we will start to study the electronic properties of the GQDs when a Coulomb potential is placed. Formation of the quasi-bound states for a supercritical potential, the bare charge of the Coulomb impurity, the four-fold symmetries, the effective charge of the impurity in different sized GQDs, the effects of disorders on the critical coupling constant, and the method of band gap measurement in triangular GQDs with zigzag edges are introduced and are discussed.

CHAPTER 3

ELECTRONIC PROPERTIES

The finite-size effect and the effect of electron-electron interactions in the presence of the Coulomb potential are discussed in greater detail in this chapter. Actually, the Coulomb impurity is placed at the center of different sized hexagonal GQDs with armchair edges. Then, the coupling strength β is gradually increased, and the response of the lowest energy electron state and a family of QBS is mainly observed within the TB and MFH models. In short, the critical coupling constant is renormalized when the electron-electron interaction is introduced, whereas the size of the vacuum has no effect on the critical threshold in both models. As an another result, the spin and valley degeneracies are not affected when a central Coulomb impurity is introduced. We also study the screening of the impurity, and the induced background charge reduces the bare charge of the impurity to the effective charge of the impurity, which is on the order of unit charge. In addition, we will examine the effects of the random disorders for atomic collapse. Basically, atomic vacancies and spatial potential fluctuations increase the critical threshold. Atomic collapse similarly observed in disordered samples at higher coupling strengths as compared to disorder-free samples. These results indicate that atomic collapse can be observed in imperfect samples such as Ar^+ ion bombarded, He^+ ion irradiated, and hydrogenated graphene.

The rest of this chapter is organized as follows. In Sec. 3.1, the finite-size effect and the effect of electron-electron interactions for the lowest bound states are discussed in greater detail. Sec. 3.2 contains screening of the Coulomb impurity by Dirac fermions. In Sec. 3.3, atomic collapse is studied in the presence of lattice distortions and spatial charge inhomogeneities.

3.1. Collapse of the Vacuum in Pristine Hexagonal GQDs

To reveal the effect of the size quantization, we systematically study a series of the pristine hexagonal GQDs with armchair edges consisting of up to 10,806 atoms (R =

10.4 nm). After this limit, physical properties approach to those of the corresponding bulk material (Li et al. (2019)). A Coulomb potential is placed at the center of each hexagonal GQDs; see the inset of Fig. 3.1(a).
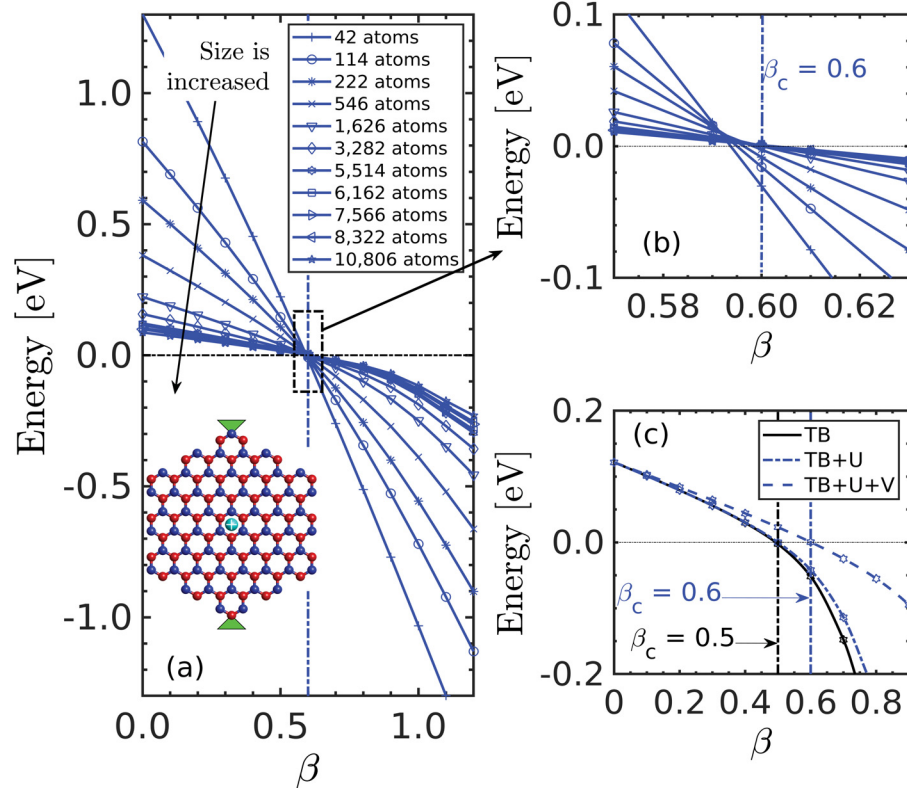
Figure 3.1. Energy eigenvalues of the lowest bound states as a function of the coupling constant β. (a) The critical coupling constant β_c is 0.6 within the MFH model for all samples that differ in size. The inset contains a sketch of the problem for the hexagonal GQD that consists of 114 atoms. Here, the sublattices A and B are red and blue filled circles, and a positively charged impurity is at the center. Green triangles show how the leads are connected to samples throughout our study to determine the transmission coefficients. (b) shows a zoomed view of the energy eigenvalues around β_c. (c) shows a comparison between the TB and the MFH models for a GQD consisting of 5514 carbon atoms.

To discuss the size effect within the MFH model, energy eigenvalues of the lowest bound states of all samples as a function of the coupling strength β and zoomed portion around the critical coupling constant β_c are shown in Fig. 3.1(a) and (b), respectively. In Fig. 3.1(a) and (b), each of the lowest angular momentum channels is doubly degenerate due to the valley symmetry (Zarenia et al. (2011); Sheng et al. (2012)). In short, the spin and valley degeneracies are preserved as a function of β. As a result, the MFH results do

not make any discrimination between the spin components due to the spin symmetry. TB results are given by the black lines, whereas the results of the spin-up and the spin-down can be followed by the red and blue lines in each of these graphs, respectively. Different kinds of symbol in Fig. 3.1(a) are attributed to the size of the hexagonal GQDs.

Each of the lowest bound states dives into the negative energies at the same value of the coupling strength that is 0.6 within the MFH model. It can be accepted as a critical point at this stage, and we will discuss this point in more detail below. It is clear that a sufficiently large sizes of these GQD is enough to observe atomic collapse due to the special characteristic of band gaps of these GQDs, as mentioned above. The collapse states are pinned at the DP as clearly shown in the experiments (Wang et al. (2013); Mao et al. (2016)). In this sense, our results indicate that the zero energy plays the same role with the DP in bulk graphene. In contrast, the FL follows the highest filled level due to a constant number of electron-like Dirac fermions. Our results pave the way for the examination of reconstruction of the Dirac vacuum within quite small sample sizes by a low computational cost.

On the other hand, the electron-electron interactions in half-filled MFH model are set by the on-site U and off-site V terms. Energy eigenvalues of the TB model are compared with those of the MFH model by setting the off-site term V to zero. As is clear from Fig. 3.1(c), the on-site term U gives no contribution to the renormalization of β_c. In contrast, the off-site term V decreases overscreening tendency (Kotov et al. (2008, 2012)) of the TB approximation by smearing out the induced charge density (Biswas et al. (2007)), and which turns out to be a 20% increase in β_c. We directly give a critical bare valance charge Z_c as follows:

$$Z_c \left(\frac{2.2}{\kappa} \right) = \beta_c \qquad \rightarrow \qquad Z_c \approx 1.64, \qquad (3.1)$$

where the dielectric constant $\kappa = 6$, and the critical coupling constant β_c equals to 0.6. It indicates that impurities with the valence charge of $Z_c \approx 1.64$ can be used to create an artificial supercritical nuclei for all GQD sizes. Our result is also consistent with the previous one in which Z_c is calculated to be larger than unit charge (Terekhov et al. (2008)). The TB result for one particular hexagonal GQD consisting of 5514 atoms shows [Fig. 1(c)] that the lowest bound state enters the supercritical regime at $\beta_c = 0.5$, which is the same as of bulk graphene. In compliance with our non-interacting fermion results, the critical wave functions of the circular GQDs merge into negative energies at the value of

$\beta_c = 0.5$ within the effective mass approximation with an infinite mass boundary condition (Van Pottelberge et al. (2017)).
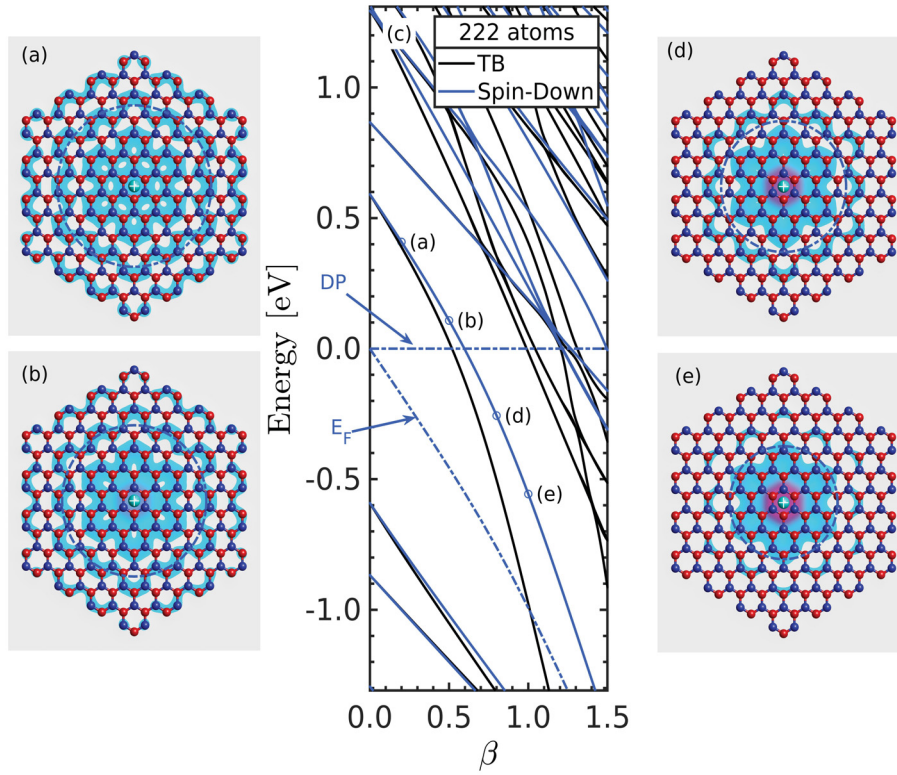
Figure 3.2. The formation of the spatially extended QBS around the impurity for the GQD consisting of 222 atoms. (c) shows the energy spectrum as a function of β. On the other hand, (a), (b), (d), and (f) show the probability density of the lowest bound state at different values of β.

When a bound state enters into the negative energy spectrum, it becomes a spatially extended resonance around the impurity. In Fig. 3.2, we show the formation of the QBS around the impurity for the spin-down fermions. Here, Fig. 3.2(a) shows the lowest energy electron state of spin-down fermions at $\beta = 0.2$. It nearly has a finite probability density at all lattice sites. Similarly, in Fig. 3.2(b), it has a equal probability density over all lattice sites. However, when β exceeds $\beta_c = 0.6$ (MFH model), the lowest energy bound state becomes a QBS, as shown in Fig. 3.2(d) and (e) for larger values of β. In Fig. 3.2(a)-(e), the dashed lines represent the characteristic length scale of the first supercritical wave function, which is calculated from the following equation $\langle r \rangle = \langle \Psi | r | \Psi \rangle$. In Fig. 3.2(c), the spectrum can be seen as a function of the coupling strength in which the DP and the FL are marked by dashed blue lines for spin-down fermions.

The band gap in the GQDs is only due to size restriction of massless Dirac fermions, and here we give an interaction-induced renormalization of β_c. This gap should not be confused with that of a gapped graphene monolayer (Zhou et al. (2007)), modelled by adding a mass term in bulk graphene (Kotov et al. (2008); Chakraborty et al. (2013); Kuleshov et al. (2015)). Reported values of β_c up to $\simeq 0.9$ (Pereira et al. (2008); Zhu et al. (2009)) are calculated for the non-interacting massive Dirac fermions, where the critical point is defined as the crossing of the collapse state with the lower continuum (Pereira et al. (2008)), instead of the DP in our calculations. In addition, the FL moves automatically down due to the absence of charge compensation, similar to our case.

In summary, the hexagonal GQDs with special characteristic band gap feature are studied by means of the TB and the MFH models. The critical coupling constant is found to be $\beta_c = 0.5$ for the non-interacting case when the Coulomb potential is placed at the center. However, β_c is renormalized to 0.6 for all sizes in the presence of off-site electron-electron interactions. It can be noted that the off-site repulsion term is responsible for this incasement in β_c due to the long-range repulsive tail. It is calculated that central impurities with the nuclear charge of $Z_c \approx 1.64$ are at the edge of the supercritical threshold. In the next section, we will study screening of the impurity in the subcritical regime.

3.2. Screening of the Coulomb Impurity in the GQDs

As the coupling strength β is increased, Dirac fermions actually screen the charged impurity by inducing the background polarization charge Q around the impurity, and which reduces the bare charge of the impurity to the effective charge of the impurity. This is known as the screening of the charged impurity, and it is experimentally accessible (Wang et al. (2012)). Here, we only restrict ourselves to the subcritical regime for both non-interacting and interacting fermions. According to Eq. 2.26 with N=2, we calculate the Q for different values of β within the TB and the MFH models. These calculations are performed at different radial distances R from the impurity to find the induced charge distribution as a function of the radial distance.

Fig. 3.3(a) for non-interacting fermions and Fig. 3.3(b) for interacting fermions show that the Q can be maximized at a specific distance from the impurity, whereas it vanishes when the summation are taken over all lattice sites. It is clear that when the

electron interactions are turned on, the Q decreases by smearing out the charge density from the impurity, in agreement with the previous theoretical calculations (Biswas et al. (2007)). Maximum value of the induced charge Q_{max} appears at R_{max} = 7a for the TB model (non-interacting fermions), and it is at R_{max} = 4a for the MFH model (interacting fermions). In addition, the maximum value of the induced charge equals Q_{max} = 0.91, which is in the unit of $+|e|$, for the TB model, and this value are found to be Q_{max} = $0.66|e|$ for the MFH model. Starting from the bare critical valance charge found in Eq.
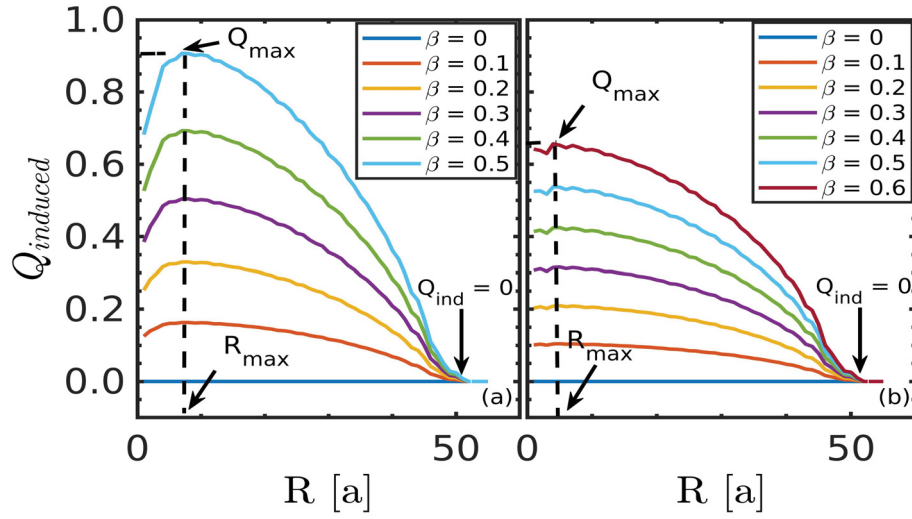
Figure 3.3. The plots show the induced charge as a function of the distance R from the impurity for a GQD consisting of 5514 atoms for the non-interacting in (a) and interacting cases in (b), respectively. Here, β values are represented by different colored lines. On the right hand side, the induced background charge is the same for spin-up and spin-down fermions due to the presence of the spin independent central Coulomb impurity.

3.1, one can calculate the effective charge of the impurity. The effective charge of the impurity for the interacting fermions can be found as follows:

$$Z_{eff} = Z_c - Q_{ind} \qquad \rightarrow \qquad Z_{eff} \approx 1. \qquad (3.2)$$

When the effective charge of the impurity is around one unit charge, and it is at the edge of supercritical regime. As for the different sized hexagonal GQDs, we also calculate the induced background charge as a function of distance from the impurity at the critical coupling constant, i.e., β_c = 0.6 (the MFH model). As is clear from Fig. 3.4(a), the different sized GQDs consisting of 1302, 5514, and 10 806 atoms have the same

maximum induced charge Q_{max} at the same R_{max}. Owing to their different sizes, the induced charge vanishes at the edge of each GQD. This also show us that the Coulomb impurity in different sized GQDs has the same value of effective charge. This finding is the our first knowledge in the current literature about the effective charge of the Coulomb impurity in the GQDs. As an another issue in bulk graphene, the non-interacting case is in a good agreement with the perturbative random phase approximation (RPA) in which the induced charge is given by $Q_{ind} = (\pi/2)\beta$, as analyzed in the previous studies (Shytov et al. (2007b); Pereira et al. (2008)). This is known as the linear screening of the Coulomb impurity by Dirac fermions in the subcritical regime. Here, we also show
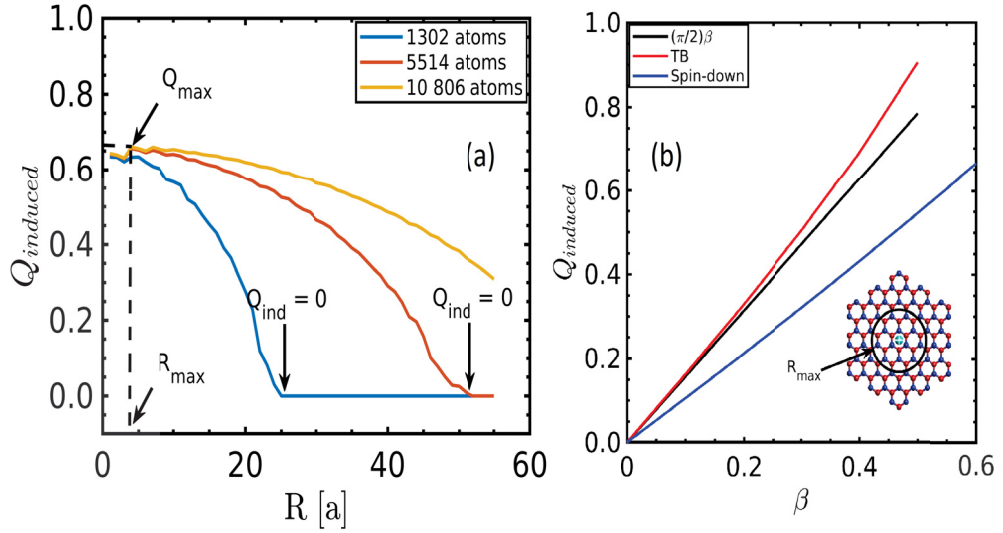
Figure 3.4. (a) The induced background charge Q as a function of the distance R from the impurity for the GQDs consisting of 1302, 5514, and 10 806 atoms at $\beta_c = 0.6$. (b) The induced background charge Q as a function of the distance β at $R_{max} = 7a$ (TB) and $R_{max} = 4a$ (MFH). Here, the GQDs consist of 5514 atoms. Black, red, and blue lines represents RPA, TB, and spin-down fermions, respectively.

that the same finding is also valid for the smaller sized GQD consisting of 5514 carbon atoms. In Fig. 3.4(b), the black line represents the induced charge according to the RPA, the red line represents the induced charge at a distance $R_{max} = 7a$ for the non-interacting fermions modelled by TB method, and similarly, the blue line is attributed to the interacting fermions such as spin-up or spin-down fermions for which R_{max} is taken as $R_{max} = 4a$. These maximum values of the distance from the impurity are taken with respect to Fig. 3.3(a) and Fig. 3.3(b) for non-interacting and interacting cases,

respectively. In the inset of Fig. 3.4(b), one can see R_{max}, which is illustrated in a smaller sized hexagonal GQD. For non-interacting case, the induced charge is in agreement with the RPA, which is known as the linear screening of the Coulomb impurity. On the other hand, for interacting case, the induced charge stays under the black line due to smearing out of the induced charge. In the charge inducement, the electron-electron interaction has a significant effect for the GQDs, and the same behaviour is presumably valid for bulk graphene (Biswas et al. (2007)).

3.3. Collapse of the Vacuum in Disordered Hexagonal GQDs

In this section, we will study the effect of vacuum imperfections. To study the effect of the lattice defects and the spatial potential fluctuations, deviations from the perfection in the vacuum are intentionally created by : (i) randomly distributed point vacancies with different concentrations and (ii) electron-hole puddles induced by Gaussian impurities. We find a strong dependence of the critical threshold on both types of disorder, leading to up to thirty-four percent increase in the critical coupling constant.

It can be useful to discuss the effect of the vacuum size from a different perspective before starting the imperfect (disordered) cases. The discrete energy levels of the pristine GQDs are summed over at the impurity site for which the radial distance is taken to be r = 0.142 nm. Here, the impurity site refers to the nearest neighbor atoms to the impurity. Such a summation corresponds to a family of QBS in which all supercritical states are sequentially arranged, and which contains the $1S_{1/2}$ state as the first component (Shytov et al. (2007a)). Atomic collapse occurs when this sharp peak in the electronic LDOS crosses just below the DP (Wang et al. (2013)), which will be the energy origin in our calculations due to the formation of spatially extended resonances at the negative energies (Van Pottelberge et al. (2017)). In the mean time, the FL moves down starting from the energy origin as the coupling strength is increased within the half-filled model (Van Pottelberge et al. (2017); Polat et al. (2020)), as previously discussed above. To avoid too cumbersome notation, the critical coupling constant of the families of QBS is represented by $\tilde{\beta}_c$, and at this stage, only the response of the spin-up Dirac fermions is studied for the perfect vacuums due to the presence of a spin-independent central potential. The spin-up QBS families at the impurity site are shown in Fig. 3.5 for the

perfect GQDs consisting of 2814, 5514, and 10 806 carbon atoms. All families are pinned
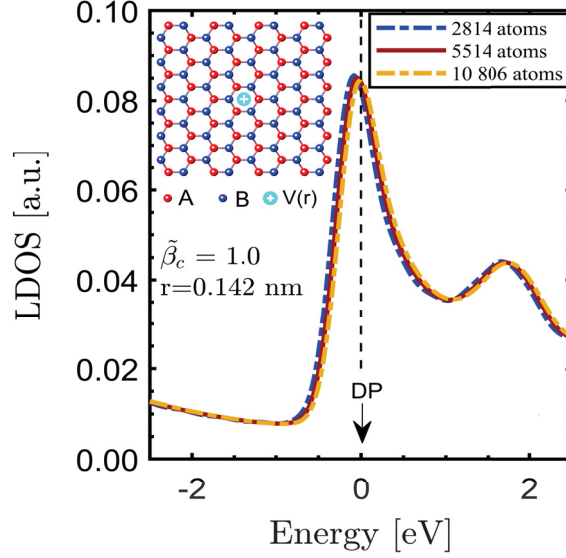
Figure 3.5. LDOS spectra at the impurity site for the numbers of 2814, 5514, and 10 806 atoms. The inset illustrates a zoomed portion of the perfect lattice with a central Coulomb impurity.

just below the DP at $\tilde{\beta}_c = 1.0$, revealing that the effect of the Coulomb impurity is the same for all these GQDs, and the critical bare valence charge is calculated to be $\tilde{Z}_c \approx 2.73$ by taking $\kappa = 6$; see Eq. 3.1.

3.3.1. Random Point Vacancies

To model lattice distortions, atomic vacancies with concentrations of 0.1%, 0.5%, 1%, and 2%, which refers to the ratio of the number of point vacancies N_{vac} to that of the lattice sites N, are created by randomly and equally removing the two sublattices, A (50%) and B (50%), of the bipartite lattice (Altıntaş and Güçlü (2018)). In this way, we create ten different disordered GQD with totaly random lattice defect configuration. When point defects are evenly distributed between the sublattices, i.e., A (50%) and B (50%), the FL continues to stay at the energy origin in the absence of the impurity (Pereira et al. (2006, 2008); Kul et al. (2020)), as shown in the inset of Fig. 3.6(b). In fact, the FL is the same for both the perfect and disordered cases that validates the previous discussion on the DP and the FL in our defect configurations when $\tilde{\beta}$ is turned on. As for the spin symmetry, it

is naturally broken in the disordered lattices (Altıntaş and Güçlü (2018)). However, there is no difference between the spin-up and spin-down families near $\tilde{\beta}_c$, as shown in Fig. 3.1(a) and Fig. 3.1(b), respectively. As is clear from these two figures, all QBS families at the impurity site retreat from the DP depending on the concentration of these defects, which are randomly distributed in the GQD consisting of 5514 atoms in the pristine case. Fig. 3.1(a) and Fig. 3.1(b) point out that $\tilde{\beta} = 1.0$ is no longer a critical coupling constant, and it is the first effect of point defects on atomic collapse.
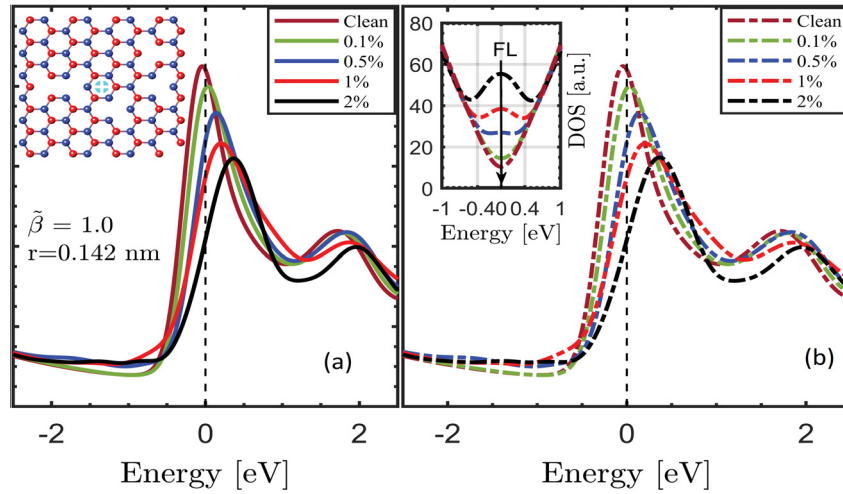
Figure 3.6. Spin-up QBS families in (a) and spin-down QBS families in (b) in the presence of finite defect densities. Inset in (a) illustrates a zoomed portion of disordered lattice with a central Coulomb impurity. The inset in (b) is the averaged spin-down DOS that marks the FL at $\tilde{\beta} = 0$.

These families transit from above to the edge of the DP at different $\tilde{\beta}_c$ which is evident in Fig. 3.7(a)-(d). The critical coupling constant gradually increases in proportion to the defect densities and reaches $\tilde{\beta}_c = 1.27$ for random dilution at 2% [see Fig. 3.7(d)]. Actually, these defects are ubiquitous in the crystal structure (Eckmann et al. (2012)). For example, the Raman spectrum has ~ 0.5 $G/2D$ intensity ratio for the high-quality graphene monolayer grown by chemical vapor deposition (CVD) (Li et al. (2009)), and this ratio indicates that there is a finite defect density in graphene. As is clear from our numerical results, these structural peculiarities can cause an increase in the critical threshold. On the other hand, the spectral shapes of all QBS families are the same as of the defect-free case, especially in the vicinity of the impurity. It can be inferred that atomic collapse can be similarly observed in the imperfect lattices with the help of a

higher valance charge.
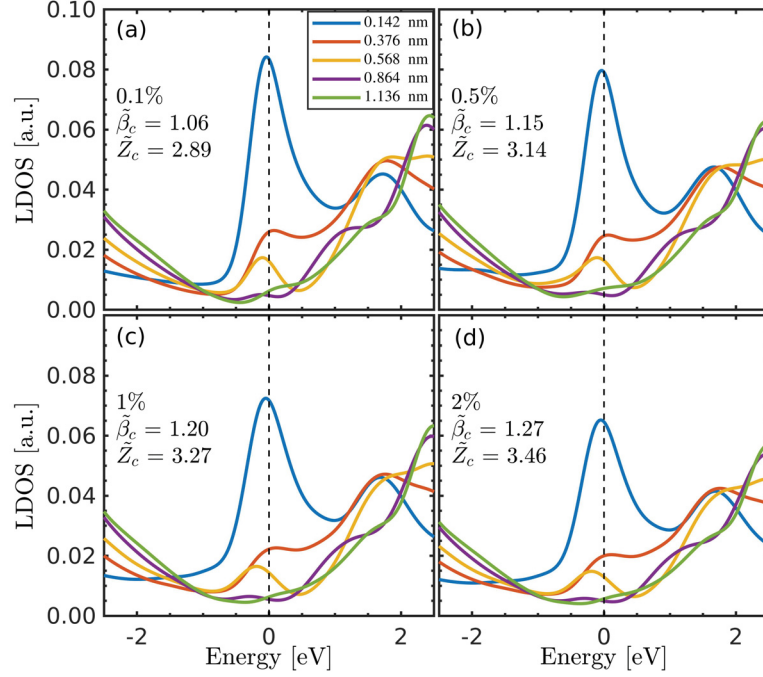
Figure 3.7. Defect-induced increase in the critical coupling constant $\tilde{\beta}_c$ for the concentrations of 0.1% in (a), 0.5% in (b), 1% in (c), and 2% in (d). The different colored lines represent the corresponding distances from the impurity.

In the half-filled Hubbard model, the lowest energy states in the conduction band are unoccupied vacancy-induced states whose energies are between 0 eV$<E<$0.4 eV for 1% defect concentration [see the global DOS in the inset of Fig. 3.6(b)]. As $\tilde{\beta}$ is increased, these states successively dive into the negative energies (not shown here). However, there is no explicit crossing from the higher energy conduction states within the energy spectrums. Therefore, of particular interest are these merging states below the DP, and the total probability density of them is calculated by p(r) = $(1/2)\left[\sum_{E<0}|\Psi(r)|^2 - \sum_{E<E_F}|\Psi(r)|^2\right]$ in which both spin components are included. For a representative sample, p(r) is projected into the space at different coupling constants, ranging from $\tilde{\beta}$ = 0.5 up to $\tilde{\beta}$ = 0.8. Response of the empty defect states below the DP to the Coulomb field for a representative sample with 1% defect density is shown in Fig. 3.8(a)-(d). It clearly shows that whenever defect states dive just below the DP, they are localized around the missing atoms by preserving their characteristic triangular shapes and then demonstrate a striking stability against the Coulomb impurity. Here, upward

36

triangular shapes belong to the unoccupied spin-up vacancy-induced states, whereas downward triangular shapes correspond to to the unoccupied spin-down defect states. On the other hand, the weight of probability density around the impurity progressively increases, but there is no formation of the first supercritical state at $\tilde{\beta} = 0.5$ nor at $\tilde{\beta} = 0.6$, which are the critical coupling constants of the $1S_{1/2}$ state for the non-interacting (Shytov et al. (2007a)) and interacting (Polat et al. (2020)) fermions in a clean vacuum, respectively. Finally, the $1S_{1/2}$ state appears at $\tilde{\beta} = 0.8$, despite not being a direct
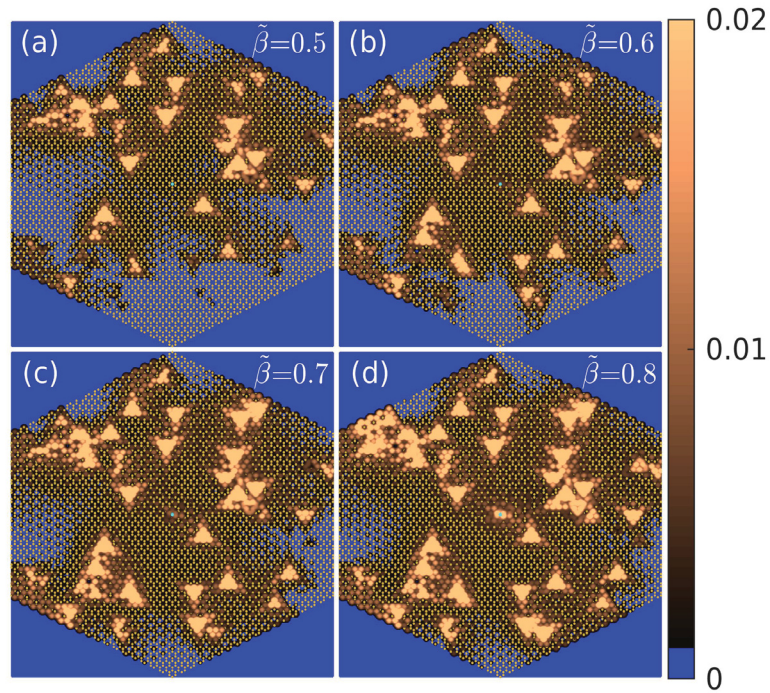
Figure 3.8. Response of the empty defect states below the DP to the Coulomb field for a representative sample with 1% defect density. Their spatial distributions are shown in (a)-(d) for $\tilde{\beta} = 0.5$, 0.6, 0.7, and 0.8, respectively. Upward (downward) triangular shapes belong to the unoccupied spin-up (spin-down) vacancy-induced states. As is clear from (d), the $1S_{1/2}$ state is formed at the center of QD marked by green dots.

contribution of the bulk states to p(r). Such a formation of the $1S_{1/2}$ state is presumably due only to the hybridized components of the diving defect states, and the defect-induced increases in Fig. 3.7(a)-(d) actually originate from the formation mechanism of the $1S_{1/2}$ state. Its shape is exactly the same as the $1S_{1/2}$ state of the defect-free GQDs, and this formation is observed for all samples at around $\tilde{\beta} = 0.8$ for random dilution at 1%.

3.3.2. Random Gaussian Impurities

We also study the effect of charge puddles on atomic collapse. In addition to 1% concentration of carbon vacancies, the electron-hole puddles are created by the superposition of contributions of randomly distributed Gaussian impurities (Bardarson et al. (2007)) with a total number of N_{imp} = 16, i.e., the impurity concentration n_{imp} = 1.1 × 10^{13} cm^{-2}. Gaussian potential at a position $\mathbf{r}_n$ can be written as follows: $V_i = \sum_{n=1}^{N_{imp}} \Delta_n \exp\left[-|\mathbf{r}_i - \mathbf{r}_n|^2 / (2\xi^2)\right]$, where Δ is the impurity strength, and the impurity correlation length is taken to be $\xi = 10a$ (a = 0.142 nm is the *C-C* distance) (Zhang et al. (2009)). Half of these impurities are chosen as positive and the other half as negative with the help of Δ, which randomly fluctuates within three different intervals: (i) $|\Delta| < 0.1t$, (ii) $|\Delta| < 0.3t$, and (iii) $|\Delta| < 0.5t$. For example, consider the case with the 1% defect concentration; we have ten different samples, each with totally random distributions. For each of these samples, we randomly distribute Gaussian impurities with $|\Delta| < 0.1t$. This is also performed for $|\Delta| < 0.3t$ and $|\Delta| < 0.5t$ in the presence of the 1% defect concentration
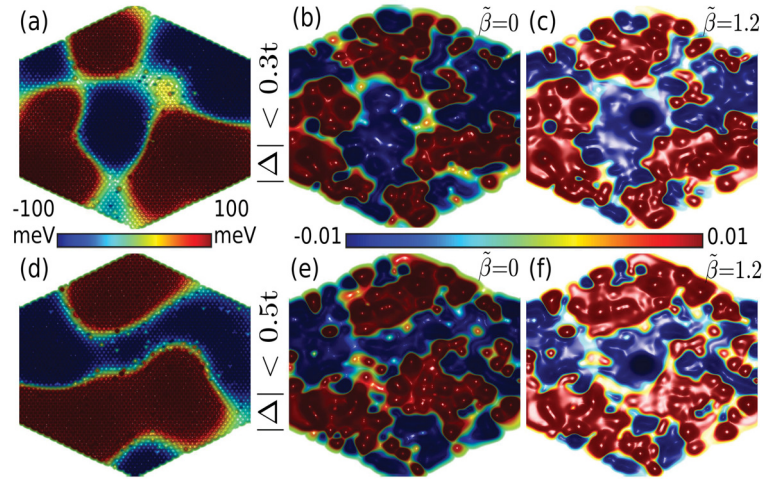
Figure 3.9. Upper panel: (a) averaged potential fluctuations for $|\Delta| < 0.3t$ (only $|\Delta|$'s averaged), (b) the total electron-hole puddles accordingly are formed at $\tilde{\beta}$ = 0, and (c) the reformation of these charge puddles at $\tilde{\beta}$ = 1.2. Lower panel: the same as the upper panel but now for $|\Delta| < 0.5t$.

Prior to the collapse experiments (Wang et al. (2012, 2013); Mao et al. (2016); Wong et al. (2017)), monolayer graphene is grown by CVD and then is transferred

onto a hexagonal boron nitride (hBN) flake placed on a SiO_2/Si substrate. To model the spatial potential fluctuations caused by such a substrate, we randomly distributed Gaussian impurities for the set of vacuum disordered by 1% concentration of carbon vacancies. The averaged potential landscapes of $|\Delta| < 0.3t$ and $|\Delta| < 0.5t$ are shown in Fig. 3.9(a) and Fig. 3.9(d), respectively. The resulting electron-hole puddles of both spin components shows that the electron puddles (red) appear in the positive potential regions, whereas the hole puddles (blue) manifest themselves in the negative potential regions as can be seen in Fig. 3.9(b) for $|\Delta| < 0.3t$ and Fig. 3.9(e) for $|\Delta| < 0.5t$. As $\tilde{\beta}$ is turned on, the charge inhomogeneities rearrange themselves under the effect of the Coulomb potential. For example, at $\tilde{\beta} = 1.2$, the electron-hole puddles of $|\Delta| < 0.3t$ and those of $|\Delta| < 0.5t$ are mapped in Fig. 3.9(c) and Fig. 3.9(f), respectively. Even if there is no significant change in the positions of the hole puddles formed at the distances away from the center, those close to the center leave their positions and are centered around the stronger Coulomb impurity. As will be seen below, such a reformation has a significant effect on the critical threshold of a family of QBS.
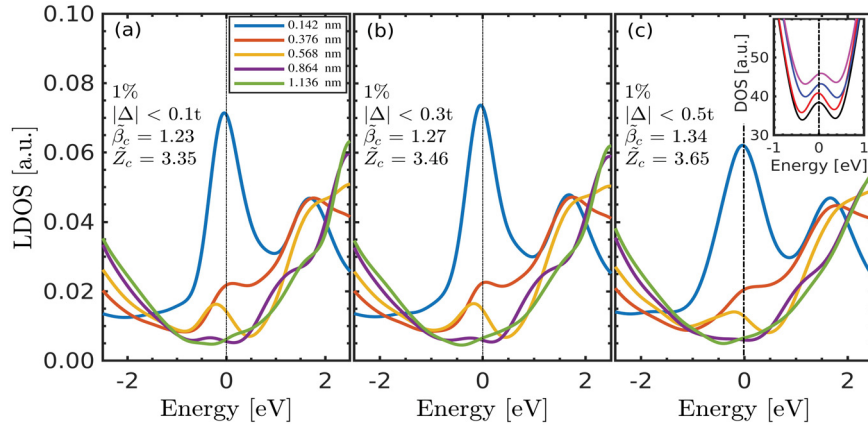
Figure 3.10. The effect of electron-hole puddles on the critical threshold in (a)-(c), which are the same for both spin components. The inset in (c) shows averaged total DOS at $\tilde{\beta} = 0$, where black, red, blue, and purple lines represent $\Delta = 0$, $|\Delta| < 0.1t$, $|\Delta| < 0.3t$, and $|\Delta| < 0.5t$, respectively. For the sake of simplicity, a space between these lines is intentionally added.

LDOS spectra in Fig. 3.10(a)-(c) are calculated for the spin-up QBS family at the corresponding radial distances, starting from the impurity site. When the positive and negative Gaussian impurities are distributed evenly, the total DOS of the spin-up fermions at $\tilde{\beta} = 0$ clearly reveal that the FL is again around the energy origin for these

configurations; see the inset in Fig. 3.10(c). There is no significant shift in the minimum energy point at $\tilde{\beta} = 0$, allowing us to take the energy origin as the DP for the non-zero values of $\tilde{\beta}$. Similar to the previous cases, whenever the sharp peak enters the negative energy spectrum, then atomic collapse has occurred. The addition of Gaussian impurities causes to an increase in the critical threshold from $\tilde{\beta}_c = 1.20$ [Fig. 3.7(c)] up to $\tilde{\beta}_c = 1.34$ [Fig. 3.10(c)], and the critical valance charge is estimated to be as high as $\tilde{Z}_c = 3.65$. In addition, we also study the point defect-free GQD consisting of 5514 atoms for ten random distributions of $|\Delta| < 0.5t$, and the critical threshold reaches to $\tilde{\beta}_c = 1.10$ (not shown here), which is $\tilde{\beta}_c = 1.0$ [Fig. 3.6(a)] in its clean case. It can be noted that the increments in the critical threshold are independent of the sign of the substrate-induced potential where the Coulomb impurity is placed and are directly proportional to the strengths of Gaussian impurities. As a result, $\tilde{\beta}_c$ seems to be highly influenced by the disorders within the vacuum itself.

In bulk graphene, a series of LDOS measurements performed by a STM reveals that a cluster, composed of four calcium dimers in the charge state of $+1|e|$, is needed to form an infinite family of QBS at just above the DP [see Fig. 1(D) in Ref. (Wang et al. (2013))]. Therefore, the critical bare valance charge should be slightly greater than $\tilde{Z}_c \gtrsim 4$ in the experiment. Accordingly, the calculated values of $\tilde{Z}_c$ are approaching to that of the experiment, and adding these experimentally relevant factors to the Coulomb impurity problem opens a new route towards such experimental results (Wang et al. (2012, 2013)). These findings can be useful in interpreting the experimental results of positively charged Coulomb impurities, even if they exceed the theoretical critical value. Results of this paper can be tested via Ar^+ ion bombarded (Lucchese et al. (2010)), He^+ ion irradiated (Chen et al. (2009)), and hydrogenated (Bostwick et al. (2009)) graphene. The latter can be achieved by transferring CVD graphene samples at different H coverages (Bostwick et al. (2009)) onto a hBN/SiO_2/Si device, which facilies to control bias and back-gate voltages. Impurities such as cobalt trimmers (Wang et al. (2012)) and calcium dimers (Wang et al. (2013); Wong et al. (2017)) can be gathered in a defect-rich region by atomic manipulation of them with the help of STM, and an artificial supercritical atom can be created from these subcritical impurities. Once the DP has been determined, LDOS spectra can be measured at different radial or lateral distances. There should be an increase in the critical threshold due to the partial removal of the π_z states.

3.4. Band Gap of the GQDs

Before starting the magnetic properties, we would like to introduce the band gap of the triangular GQDs with zigzag edges, and it will be compared with that of the hexagonal GQDs with armchair edges. As explained above, the hexagonal GQD has a special band gap property, which corresponds to the confined Dirac fermions. However, the triangular
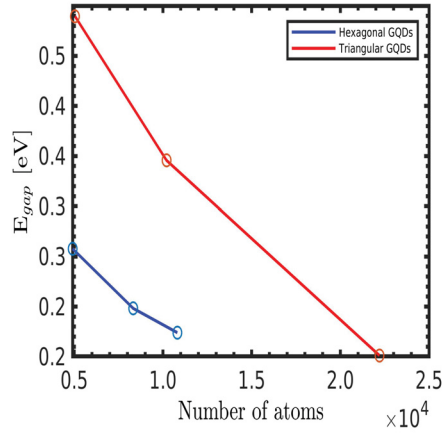
Figure 3.11. The band gap of different sized hexagonal and triangular GQDs with armchair and zigzag edges, respectively.

GQDs with zigzag edges have band gap due only to the size restriction. Owing to the presence of the localized edge states at around the Fermi level, it is not easy to exactly determine the band gap of the triangular GQDs, especially within the mean field Hubbard model. Since the onsite Coulomb interaction separates these edge states from the FL as opposed to the TB model. To overcome this difficulty and to find the band band gap in the presence of the localized edge states, we calculate the band gap of the triangular GQDs with zigzag edges by measuring LDOS at the center atom, which has minimum edge state probability. In this way, the probability density of the edge states at around the FL is reduced, and only the states with bulk state character become apparent. Such a local calculation allows us to obtain the band gap for this particular energy spectrum by suppressing and eliminating the edge states at around the FL.

Fig. 3.11 shows us the band gaps of different sized hexagonal (blue line) and triangular (red line) GQDs. The band gap in the triangular GQDs is the same for the MFH and TB models. It means that there is no direct effect of the interactions within

the mean field approximation. The triangular GQDs have a band gap, which is always smaller than that of the hexagonal GQDs.
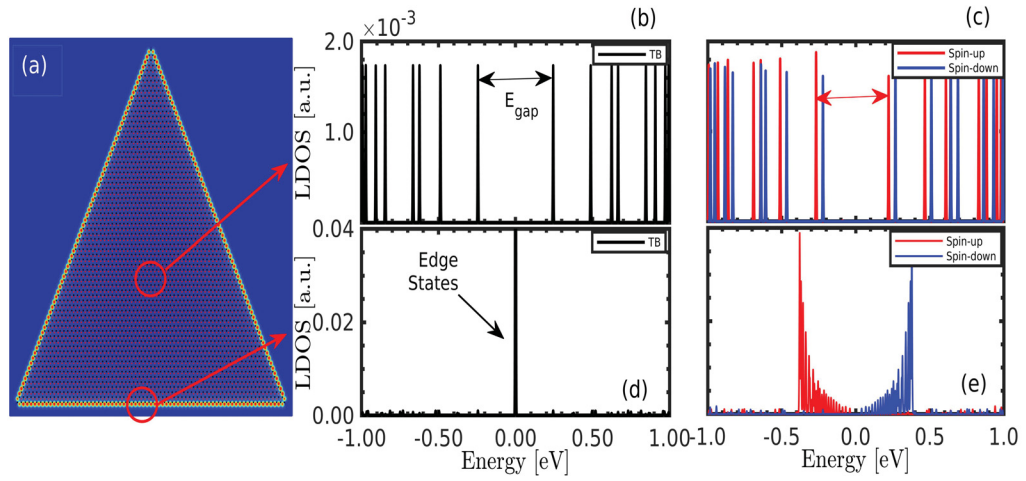
Figure 3.12. (a) Spin density of the triangular GQDs consisting of 5038 atoms, (b) and (c) show band gap for the TB and the MFH model with respect to central atom, (d) and (e) show the edge states and their related symmetries.

As is clear from Fig. 3.12(a), the spin density shows that the edge state are localized at the edge of the QD consisting of 5038 atoms. These edge states lead to ferromagnetic ground state of the triangular GQDs. We measure the LDOS to find out the band gap of these GQDs within the both models. When we measure the LDOS at the central atom within the tight binding model [Fig. 3.12(b)], the band gap clearly appears. The same approach is used for the MFH model, and the same result has been obtained, please see Fig. 3.12(c). As for the edge states, we calculate the LDOS at the edge of the triangular GQD. As shown in Fig. 3.12(d), all of the edge states localize at the FL within the TB model. They create a degenerate state at the FL. On the other hand, the mean field Hubbard model separates these states away from the FL with the help of onsite Coulomb repulsion, and there is a symmetry between the spin-up and spin-down fermions, which can be clearly seen in Fig. 3.12(e). In the STM measurements, one can measure the edge states by fixing the bias voltage at around the FL. Similarly, by fixing the STM tip at a specific region, one can directly measure the band gap of the triangular GQDs by changing the bias voltage value. It will gives an energy spectrum free from the edges states, which remove the complication of the energy spectrum.

From now on, we will examine the magnetic properties of the GQDs in the

presence of the charged impurities. A special attention has been paid to a charged vacancy, which is responsible for the recovering of the spin symmetry, as we will discussed in the next chapter. As for the triangular GQDs, we also study the single charged vacancy placed at the center. First, we will discuss the spin splitting in these GQDs with the help of local calculations. Second, we will show that the local magnetic moment induced by a bare carbon vacancy can also be adjusted in these GQDs by charging the carbon vacancy (Mao et al. (2016)).

CHAPTER 4

MAGNETIC PROPERTIES

In this chapter, we study a single charge vacancy, which is equivalent to pulling up many charged ions and can be realized in an experiment (Mao et al. (2016)). We calculate the spin and valley splittings for a bare vacancy in different sized hexagonal GQDs with armchair edges, after that, we follow these splittings by charging the single carbon vacancy. Such splittings can be measured experimentally as mentioned in Sec. 1.4 via STM. The effect of charging the vacancy on these splittings are discussed in our previous paper (Polat et al. (2020)). In addition, we obtain the spin splitting in triangular GQDs with zigzag edges in this chapter.

The rest of this chapter is organized as follows. In Sec. 4.1, the spin and valley splittings are investigated in greater detail. In Sec. 4.2, state characteristics in the presence of a bare and charged vacancy are studied. Sec. 4.3 introduces the spin splitting in triangular GQDs with zigzag edges.

4.1. Spin and Valley Splittings

The breaking of the four-fold symmetry in nanographene and related structures is a vital importance in understanding the electronic as well as magnetic properties. In this sense, we analyze the sublattice-induced symmetry breaking staring from the pristine hexagonal GQDs. DOS obtained for the clean hexagonal GQD consisting of 5514 atoms using the TB model shows that the highest (lowest) occupied (unoccupied) state in the valence (conduction) band is doubly degenerate [Fig. 4.1(a)]. It can be noted that all sizes have the same valley symmetry (Güçlü et al. (2014)), and the valley degeneracy is observed in both the TB and the MFH models in the same way.

When a single carbon defect is intentionally created by removing of the π_z orbital of the sublattice A from the central benzene in the hexagonal GQDs with armchair edges, the broken symmetry of the valley states shows itself as the valley splittings with equal magnitude in electron and hole channels within the TB method, see the vertical arrows in

Fig. 4.1(b). At the FL, we have a pronounced vacancy peak due to intervalley scattering caused by a bare carbon vacancy. This vacancy state splits into up and down vacancy states with equal spin probability and the occupation of $<n_\downarrow> = 1$ and $<n_\uparrow> = 0$ as shown in Fig. 4.1(c) when the electron-electron interactions are turned on within the MFH model. These vacancy peaks are symmetrically located with respect to Fermi level,
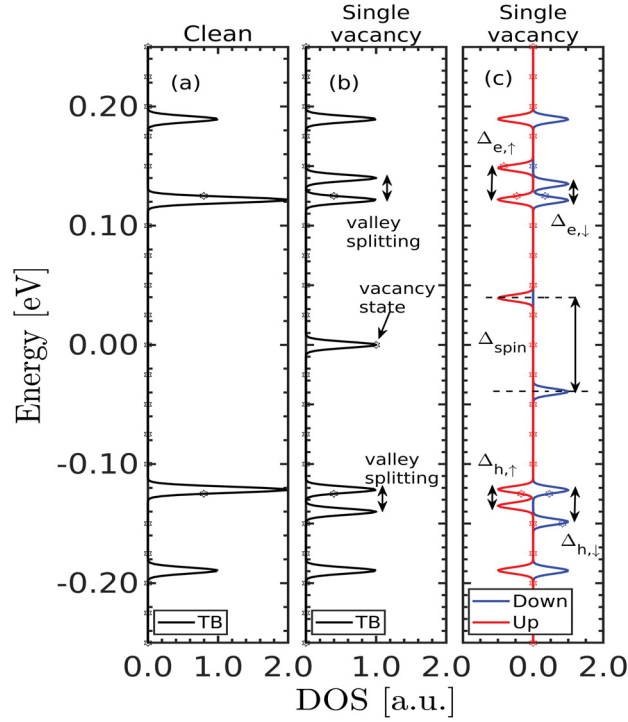
Figure 4.1. (a) total densities of states are shown for a pristine hexagonal GQD consisting of 5514 atoms, (b) total TB DOS belongs to the same GQD that contains a bare vacancy placed near the center, and (c) contains the spin and valley splittings for both spin components.

and the spin splitting Δ_{spin} between them is found to be 78 meV for this particular GQD. This splitting, also known as the spin polarization, is proportional to the on-site Coulomb repulsion U (González-Herrero et al. (2016)). When it comes to the valley splittings, the picture becomes much more complicated. Note that the total DOS distribution of the spin-up contains two nonequivalent valley splittings. In the electron channel, we have the valley splitting $\Delta_{e,\uparrow}$ of 26 meV. In the hole channel, the valley splitting $\Delta_{h,\uparrow}$ is found to be 13 meV. Similarly, the total DOS distribution of the spin-down has two unequivalent valley splittings in both channels. Interestingly, there is an additional symmetry related to the valley splittings dictated by the electron-hole symmetry. In the presence of a bare

vacancy on the A sublattice, that is given by

$$\Delta_{e,\downarrow} = \Delta_{h,\uparrow}, \qquad \Delta_{h,\downarrow} = \Delta_{e,\uparrow}. \qquad (4.1)$$

As yet there is no discussion on the effect of the size on the splittings. To analyze the size dependence, the spin and valley splittings are plotted as a function of the size of the hexagonal GQDs in Fig. 4.2(a). It is clear that the valley splittings dominate the spin splitting at small sizes. On the contrary, for larger sizes, the valley splittings are quite small as compared to the spin splitting in the presence of a single bare vacancy. Moreover, the additional symmetry between the valley splittings, given in Eq. 4.1, is conserved as a function of the size [see the overlapping lines in Fig. 4.2(a)].
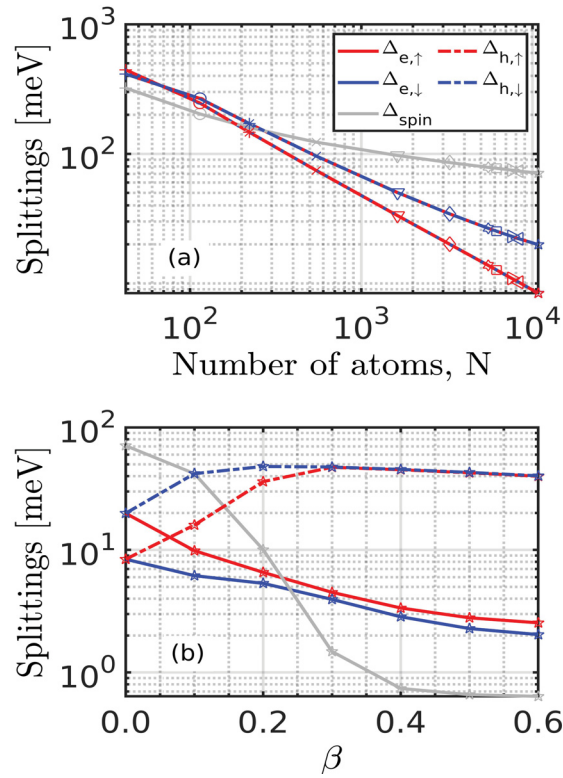
Figure 4.2. (a) clearly shows the spin and valley splitings as a function the size of the hexagonal GQDs. (b) the spin splitting disappears as a function of β, while the valley splittings do not completely vanish.

When the vacancy is positively charged with the Coulomb potential, the spin splitting decreases as a function the coupling strength β as shown in Fig. 4.2(b) for the hexagonal GQD consisting of 5513 atoms. The quenching of the spin splitting occurs at the coupling strength of $\beta = 0.4$ that lies in the subcritical regime. It mimics that the

local magnetic moment can be tuned with the help of a charged vacancy. The situation is totaly different in the valley splittings depending on the occupation of the states. While the valley splittings of $\Delta_{h,\uparrow}$ and $\Delta_{h,\downarrow}$ increase as a function of the coupling strength, both $\Delta_{e,\uparrow}$ and $\Delta_{e,\downarrow}$ show a decrement. However, all valley splittings continue to exist. As it is clear, the spin splitting has a different behaviour from that of the valley splittings for a charged vacancy, and which could prevent the valley states mixing with the spin states. Such a behaviour can be used to create new types of spintronic devices in the near future.

4.2. State Characteristics

The TB energy spectrum of a GQD consisting of 5513 atoms is plotted in Fig. 4.3(a) as a function of β. The vacancy state, labelled as (c) in Fig. 4.3(a), is pinned at the energy origin and dives immediately into negative energies when the carbon vacancy is charged. From top to bottom, the spatial distributions of the π_z-derived state are shown in Fig. 4.3(c) for the following values of $\beta = 0$, 0.1, 0.2, and 0.3, respectively. When we zoomed into the bare defect [at the top of Fig. 4.3(c)], the triangular interference pattern due to intervalley scattering can be seen as a characteristic spatial shape (Ugeda et al. (2010)). As β is increased, the intervalley scattering is gradually surpassed by the interband scattering, and finally the uniform distribution of the vacancy state takes place at the $\beta = 0.2$ and 0.3. It means that highly localized defect state returns to its original bound state characteristic; however, these scaled figures render the uniform spatial distribution invisible. This particular behaviour will be strengthened by means of the transmission coefficients in the next chapter.

The spatial extension of the state labeling as (d) is shown in Fig. 4.3(a). From top to bottom, Fig. 4.3(d) exhibits the spatial extension of the critical state around the vacancy for $\beta = 0$, 0.3, 0.6, 0.8, and 1.0, respectively. Uniform spatial extension of the critical state exists for $\beta = 0$ as shown at the top of Fig. 4.3(d). On exceeding the critical value, $\beta \gtrsim 0.5$, the critical state dives into negative energy spectrum, so that the appearance of the quasi-localized state occurs around the charged vacancy. It is actually defined as the counterpart of the 1S atomic collapse state (Mao et al. (2016)).

When the electron interactions are turned on, we have a different picture. The energy spectrum of the spin-up is superimposed to that of the spin-down in Fig. 4.4(a)
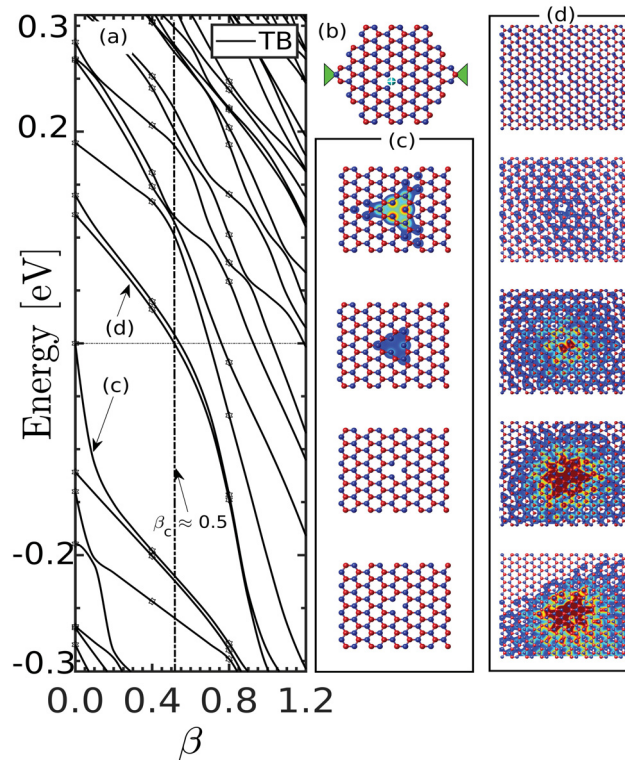
Figure 4.3. The energy spectrum of TB model as a function of the β is shown in (a). The positions of the leads and the bare carbon vacancy are sketched in (b). Scaled electronic densities per lattice of the vacancy state, i.e., LDOS, for the $\beta = 0$, 0.1, 0.2, and 0.3 can be seen in (c), from top to bottom. The quasi-localization of the lowest bound state is demonstrated in (d) for the $\beta = 0$, 0.3, 0.6, 0.8, and 1.0, from top to bottom.

as a function of β. If Fig. 4.4(a) is carefully analyzed, the spin symmetry does not exist up to $\beta = 0.4$. In other words, an exact overlap of the energy spectrums occurs at $\beta = 0.4$ meaning that the spin symmetry is regained for the larger coupling strength values, as previously discussed. There is a defect state in the spin-up spectrum that is labelled as (b) in Fig. 4.4(a). Its spatial distribution is displayed in Fig. 4.4(b) for $\beta = 0$, 0.2, and 0.4 starting from the top. The defect state in the spin-up spectrum merges into negative energies when β exceeds 0.1. The ideal triangular interference pattern characteristic starts to decay, indicating a uniformly distribution on the lattice sites. On the other hand, the defect state in the spin-down spectrum loses its triangular shape from the moment the vacancy begins to charge, and similarly it has a uniform distribution at $\beta = 0.4$ as shown at the bottom of Fig. 4.4(c). At a value of $\beta = 0.7$, both spectrums have new diving levels; see in Fig. 4.4(a). Both of the critical states become quasi-localized states in the

supercritical regime as displayed in the right columns for spin-up (d) and spin-down (e) states for $\beta = 0$, 0.7, and 1.2, from top to bottom, respectively. As compared to the non-interacting case, the critical coupling constant is renormalized to $\beta_c = 0.7$ in the presence of electron-electron interactions for the charged vacancy. The critical states in both energy spectrums collapse at the same value of β_c. It can be noted that the values of β_c, discussed in this section, are valid for all sizes of the hexagonal GQDs when a vacancy is charged with the Coulomb potential.
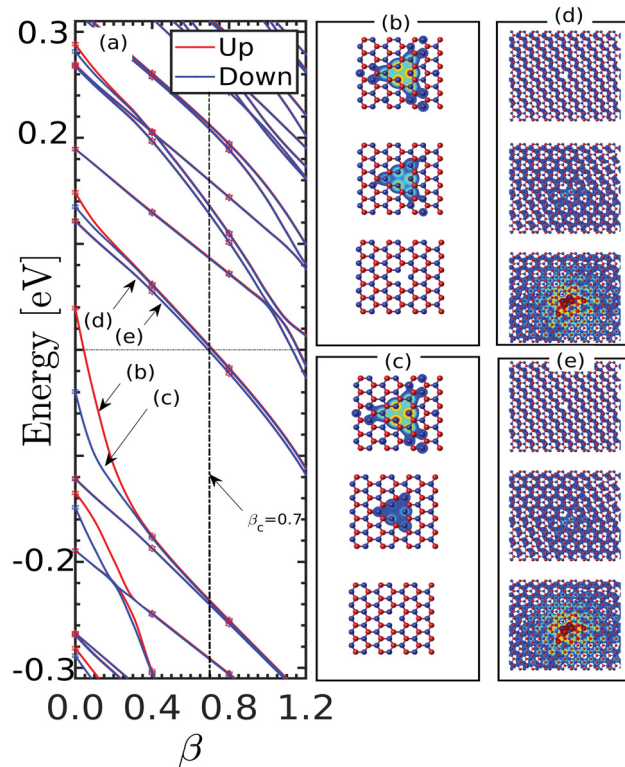
Figure 4.4. The energy spectrums of the spin-up and spin-down are shown in (a). Scaled electronic densities for the vacancy states can be seen in (b) and (c) for $\beta = 0$, 0.2, and 0.4, from top to bottom. In (d) and (e), the behaviour of the critical states for β values of 0, 0.7, and 1.2 can be seen starting from top.

The behavior of the staggered magnetization as an order parameter of the antiferromagnetism is also discussed for different values of the coupling strength. As plotted in Fig. 4.5, the staggered magnetization μ_s^z decreases as a function of β and nearly vanishes when the coupling constant equals $\beta = 0.4$. This behaviour guarantees that the spin symmetry is regained by reducing an order of the antiferromagnetism. This result strengths our previous findings related to the charging of a vacancy. In this manner, the

mechanisms of evolution observed for the vacancy states in the presence of a charged vacancy seem to be the underlying reason.

In summary, it is revealed with the help of total DOS calculations that a bare vacancy gives rise to the simultaneous formation of the valley and spin splittings in the hexagonal GQDs with armchair edges. In particular, for larger sizes, the spin splitting is larger than the valley splittings, whereas the valley splittings become dominant for the smaller sized hexagonal GQDs. As the coupling strength β is increased, the spin splitting gradually decreases and finally vanishes at $\beta = 0.4$. As an additional result, the behaviour of valley splitting under the Coulomb field completely depend on the occupation of the valley states. In the hole (electron) channel, the valley splittings show
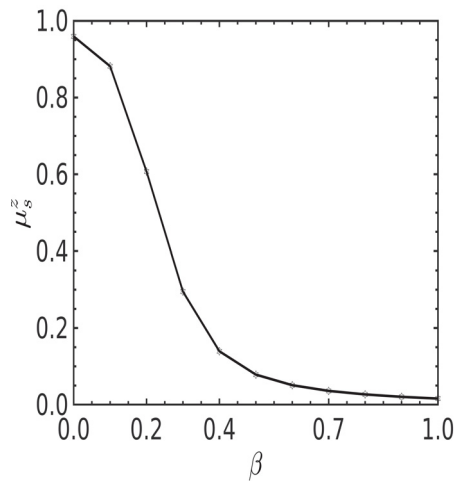
Figure 4.5. The quenching of staggered magnetization μ_s^z, which is given as a function of the coupling strength β.

an increment (decrement) for the larger coupling strength. However, the valley splittings in both channel never vanish as opposed to the spin splitting. It signals that the mixing of the valley states with the spin states is not possible in the presence of a charged vacancy.

4.3. Spin Splitting in Triangular GQDs

In triangular GQDs with zigzag edges, the degenerate edge states appear at the FL in the tight binding energy spectrum. This actually makes difficult to specify the defect state when a bare carbon vacancy is introduced to the structure, since the defect

state similarly shows itself at the FL within the TB model. To overcome this issue, we utilize the local density calculations, which is of our main interest in this section. When a triangular GQDs are constructed with the edge atoms belong to the sublattice A, the central atom appears as a type B atom. In Fig. 4.6(a), one can see that the edge atoms has a net magnetic moment, i.e., the edge spin density, whereas the local magnetic moment induced by a bare carbon vacancy can be seen at the center of the GQD. Here, the bare carbon vacancy belongs to the sublattice B, and the triangular shape is the characteristic shape of a single carbon vacancy. When the local density of state calculation is performed for the nearest neighbour atoms of the bare vacancy, Fig. 4.6(b) shows that the only single defect state shows itself at the center of the energy spectrum within the TB method, which is a direct result of the suppression of the edge states at the center. When electron interactions are turned on within the mean field approximation, the spin-up and the spin-down defect states separately appear in the negative and positive energy channels, respectively. This is actually due to the intervalley scattering caused by a single carbon vacancy. The distance between them in the energy scale is known as
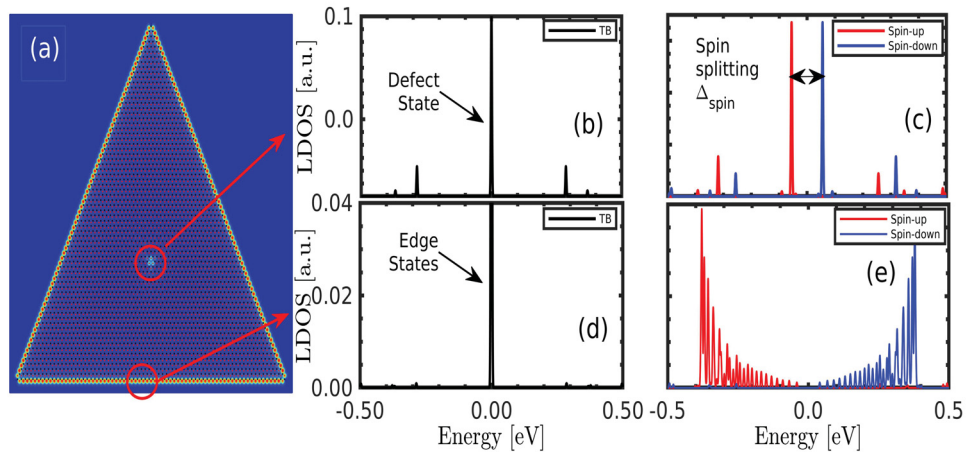
Figure 4.6. (a) shows the spin density of the triangular GQDs consisting of 5037 atoms at the edges and the characteristic shape of the bare carbon vacancy, (b) and (c) show the defect states for the TB, spin-up, and spin-down fermions in the local calculations, and (d) and (e) show the symmetrical formation of the edge states, even in the case of a bare vacancy.

the spin splitting, whose magnitude will be given below. When the same calculations are performed for the edge states, the result within the TB model [Fig. 4.6(d)] should show the edge states, but it is not entirely clear whether they are edge states or defect states. On

51

the other hand, with the help of on-site Coulomb repulsion, the MFH model as shown in Fig. 4.6(e) guarantees that these states are the edge states, and these states are arranged symmetrically around the Fermi level.

As for the relation between the spin splitting and the size of the triangular GQDs, the spin splitting decreases when the size of the GQDs is increased. It means that it is not easy to measure the spin splitting in bulk samples, and such a measurement can be easily performed in the finite sample sizes, as previously done in the GQDs (Freitag et al. (2016, 2018)). When the different sized triangular GQDs are considered, the spin splitting as a function of size of the triangular GQDs is given in Fig. 4.7. This figure shows that the magnitude of the spin splitting is closely related with the size of the GQDs, and it is about 100 meV for the triangular GQD consisting of nearly 10,000 atoms. As a comparison, the spin splitting in the triangular GQDs is larger than that of the hexagonal GQDs, see the spin splitting in the hexagonal GQDs in Fig. 4.2(a). The nearly same atom number in hexagonal GQDs has approximately 70 meV spin splitting in the presence of a bare vacancy, and it disappears when the vacancy is charged. However, as we previously introduced in Sec. 4.1, the valley splitting continues to exist for the hexagonal GQDs with armchair edges. The valley splitting in the triangular GQDs is not considered in this thesis.
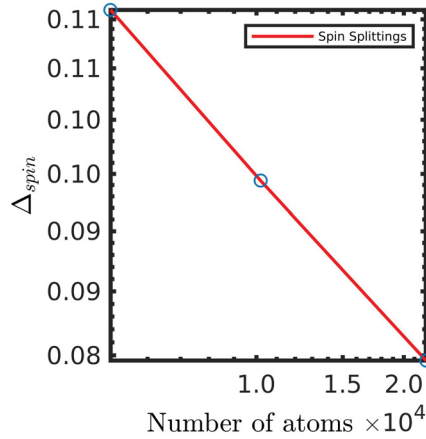

Figure 4.7. The spin splitting in different sized triangular GQDs with zigzag edges. When the size of the GQDs is increased, the spin splitting decreases according to the local density of state calculations. Δ_{spin} is on the order of eV.

The same charging process has been applied to the bare vacancy, which is at the

center of the triangular GQDs consisting of 5037 atoms. The vacancy is charged with the Coulomb potential by gradually increasing the coupling between the impurity and the graphene lattice. As the charge state of the vacancy is increased, the local magnetic moment starts to disappear in the subcritical range, as similar to what we observed in the hexagonal GQDs. As shown in Fig. 4.8(a)-(c), we calculate spin densities at different coupling constants of $\beta = 0$, 0.2, and 0.4, respectively. This figure is scaled with respect to $\beta = 0$ in each case. There is no change for the edge magnetism in these triangular GQDs, even in the case of different coupling strength values, which is evident in Fig. 4.8(a)-(c). When a point vacancy is charged with the Coulomb potential, the edge magnetism persist, but on the other hand, the local magnetic moment induced by a bare point vacancy gradually weakens as a function of the coupling strength, and it disappears at $\beta = 0.4$. This result is in compliance with the our previous findings for the hexagonal GQDs and indicates that the local magnetic moment can be adjusted by charging a vacancy (Mao et al. (2016)). The main point related with this result is that the defect states regain their original bound state characteristics when a vacancy is charged with the Coulomb potential.
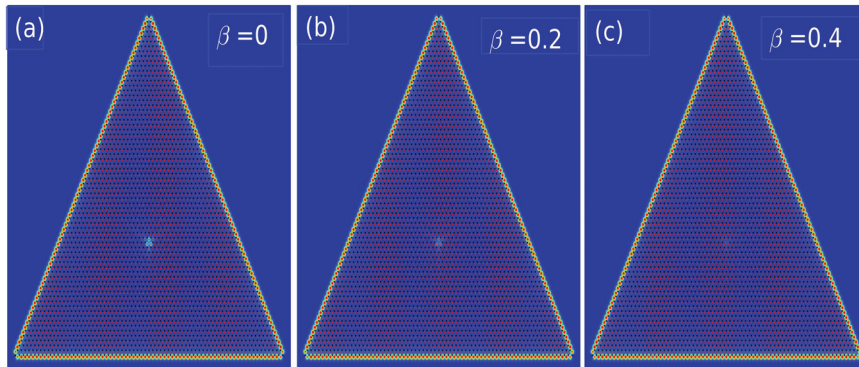
Figure 4.8. (a) Spin density of the triangular GQDs consisting of 5037 atoms shows that the edge magnetism and the triangular shape of the local magnetic moment at $\beta = 0$, (b) and (c) are the same, but now at $\beta = 0.2$ and $\beta = 0.4$, respectively.

In short, the formation of the quasi-localized state around a charged vacancy is monitored with the help of LDOS. The critical state appears when the coupling constant exceeds $\beta_c \approx 0.5$ for TB and $\beta_c = 0.7$ for the MFH models for a charged vacancy. On

the other hand, the local magnetic moment disappears when the vacancy is charged with the Coulomb potential, i.e., regaining of the spin symmetry. The quenching of the spin splitting is also discussed with the help of the staggered magnetization, which reinforces the findings related to regaining of the spin symmetry. As we will show in the next chapter, the transmission coefficient of the first critical states stays the same in the subcritical regime, but it decreases in the supercritical regime. On the contrary, those coefficients of the vacancy states increase in the subcritical regime as a function of the coupling strength, but they remains the same in the supercritical regime.

CHAPTER 5

TRANSPORT PROPERTIES

In this chapter, we will closely examine the transmission coefficients of the lowest bound states of the different sized hexagonal GQDs in the presence of two impurity configurations: (i) a central Coulomb impurity and (ii) a charged vacancy near the center. In both the TB and the MFH models, we will show that a sudden downshift in the transmission peaks shows a clear signature of the transition from subcritical $\beta < \beta_c$ to supercritical $\beta > \beta_c$ regime.

The rest of this chapter is organized as follows. In Sec. 5.1, transmission coefficients of the lowest bound state are studied in the presence of a central Coulomb impurity in different sized hexagonal GQDs. In Sec. 5.2, transmission coefficients of the lowest bound state and the defect state in the presence of a charged vacancy are examined for different coupling strength values.

5.1. Transmission Coefficients of the Lowest Bound State

As a starting point, we will examine the transmission coefficient of different sized hexagonal GQDs in the presence of a central Coulomb potential. The transmission coefficients T of the lowest bound states as a function of the energy E are shown in Fig. 5.1(a), (b), and (c) for the hexagonal GQDs consisting of 546, 1,626, and 10,806 atoms, respectively. In all figures, from left to right, each of the transmission peaks is numerically calculated for the consecutive values of β with a step size of 0.1, starting from the $\beta =$ 0. When the subfigures are compared with each other in the absence of the Coulomb potential, i.e., $\beta = 0$, it is clear that the transmission coefficients of the lowest bound spin-down states decrease inversely with the size of the GQDs and reaches its minimum for the GQD that contains 10 806 atoms. It can be noted that the maximum transmission is observed for the all GQDs consisting of up to 222 atoms, i.e., T = 1. In the subcritical range $0 < \beta < \beta_c$, the transmission coefficients do not make significant changes. In other words, the transmission coefficients of the lowest bound states remain almost the

same in the subcritical regime due to the absence of the backscattering in the presence of a central Coulomb impurity, in agreement with the previous theoretical calculation (Novikov (2007)). On the other hand, when the coupling strength exceeds the critical value of $\beta_c = 0.6$, those coefficients drop immediately because of the collapse of the wave functions. In other words, the lowest energy electron states become the $1S_{1/2}$ state of the impurity with a spatial localization, which is known as the graphene version of atomic collapse. The peak values of the transmission coefficients are plotted as a function of the
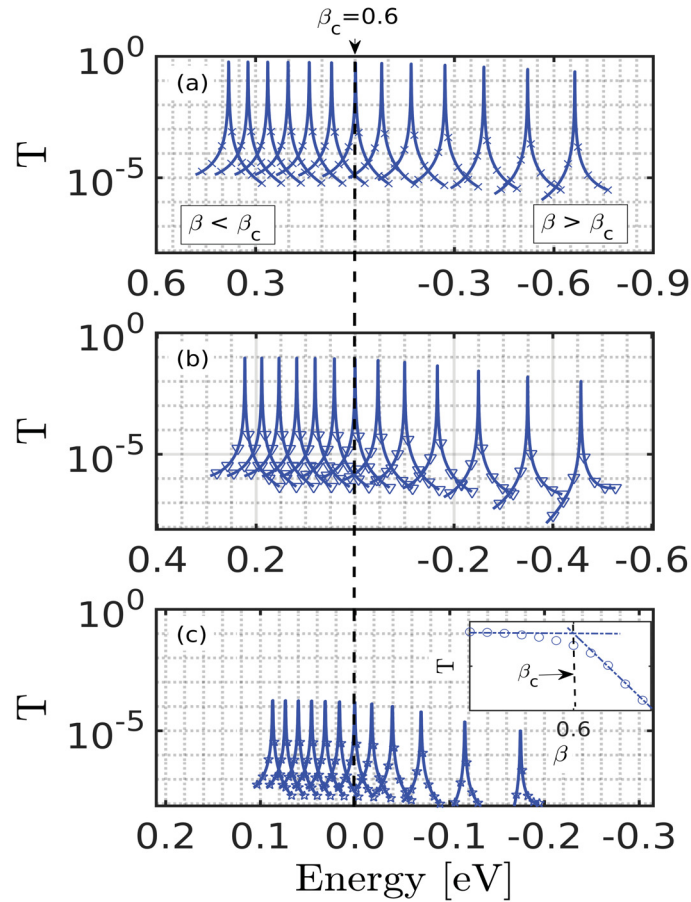
Figure 5.1. The transmission coefficients of the MFH model in (a), (b), and (c) for the number of 546, 1,626, and 10,806 atoms, respectively. The behaviour of transmission coefficients obviously corresponds to two different regime: (1) $\beta < \beta_c = 0.6$ is the subcritical regime and (2) $\beta > \beta_c = 0.6$ is the supercritical regime. Inset in (c): the critical coupling constant β_c is at the point of intersection of two lines on a linear scale.

coupling strength β in the inset of Fig. 5.1(c) for the GQD consisting of 10 806 atoms. Two different regime are represented with the lines, and the point of intersection clearly

exhibits β_c.

As for the TB model, we also calculate the transmission coefficients for the GQDs consisting of 5514 atoms. Fig. 5.2(a)-(c) show the energy eigenvalues of the TB and MFH models as a function of the coupling strength β, the transmission coefficients of the lowest energy state for TB model, and the transmission coefficients of the lowest energy state for the MFH model. Fig. 5.2(b) shows that whenever the lowest energy electron state dives below the zero energy, i.e., below the DP, those coefficients immediately decrease. It basically reflects the formation of the spatially extended resonance around the impurity. In addition, it is well-known that its width increases when such a state turns into a QBS in the supercritical regime, which happens at $\beta_c = 0.5$ for the TB model (black lines), as shown in Fig. 5.2(a). As previously mentioned, and as shown in Fig. 5.2(a), the same
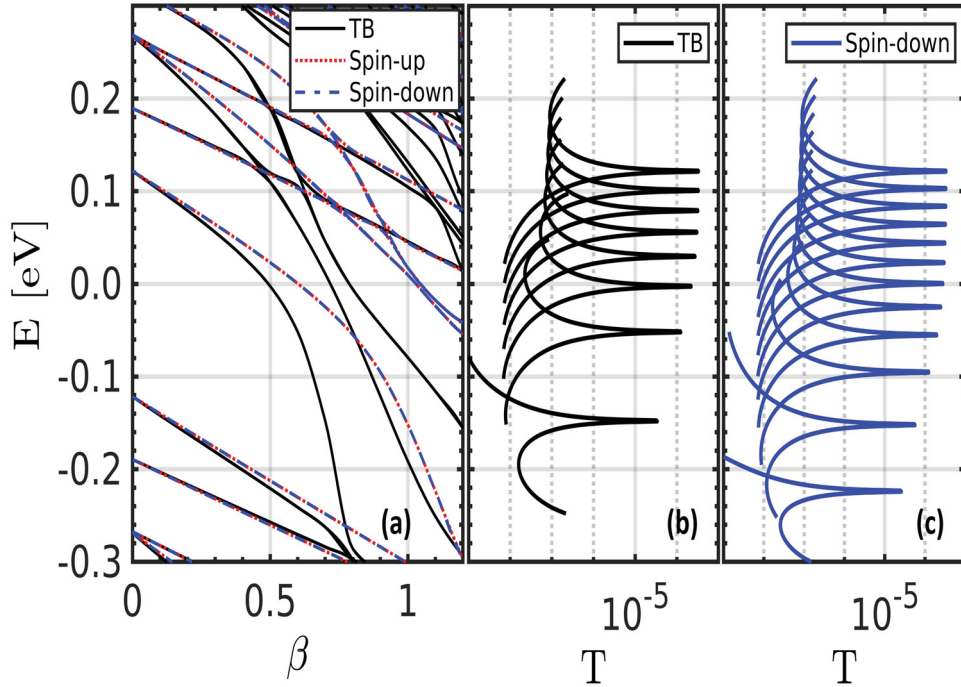
Figure 5.2. For the GQDs consisting of 5514 atoms, (a) shows the energy eigenvalues of the TB and MFH models as a function of the coupling strength β. (b) shows the transmission coefficients of the lowest energy state for TB model, and (c) shows the same but now for the MFH model.

coefficients within the MFH model (red dashed line for spin-up and blue dashed line for spin-down fermions, respectively) suddenly decrease when the lowest energy state dives below zero energy for which $\beta_c = 0.6$ is the critical coupling constant. This can be seen in Fig. 5.2(c) for spin-down fermions.

5.2. Transmission Coefficients for a Charged Vacancy

After the bare vacancy charged with the subcritical and supercritical Coulomb potential, the transmission coefficients of the critical states of TB model, spin-up, and spin-down spectrums of the MFH model are numerically calculated. First of all, in Fig. 5.3(a), (c), and (e), the transmission coefficients are approximately 2×10^{-4} in the subcritical regime $\beta < \beta_c$. It can be inferred that there is no a direct effect of including electron-electron interactions within the mean-field approximation on the transmission coefficients of the lowest bound states. Whenever a critical state dives into the negative energies, which happens at the $\beta_c \approx 0.5$ for TB and $\beta_c = 0.7$ for the MFH spectrums in the presence of a charged vacancy, the transmission coefficients of the lowest bound sates immediately drop. Basically, the quasi-localized character of these states is responsible for the decrement observed in transmission coefficients.
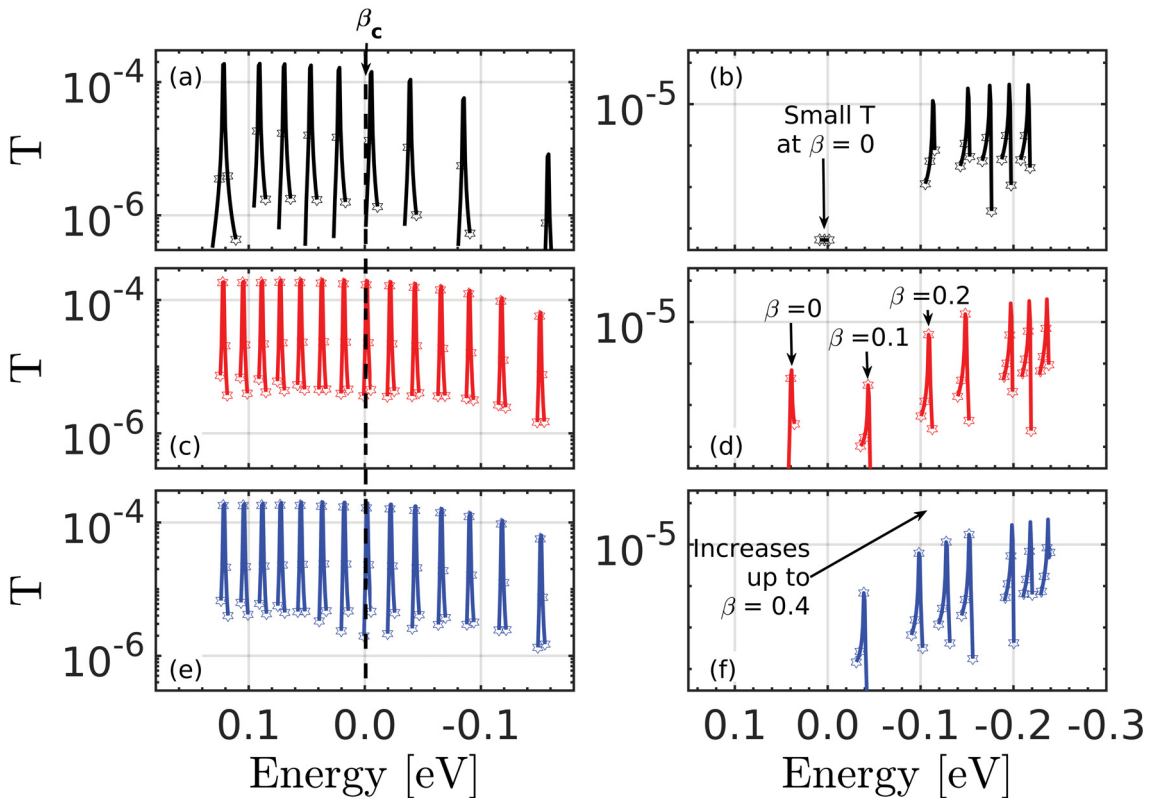
Figure 5.3. Transmission coefficients of the critical states of TB in (a), spin-up in (c), and spin-down in (e) spectrums are plotted. The vacancy states in (b), (d), and (f) can be seen as a function of energy.

The transmission coefficient of the vacancy state in TB spectrum is plotted in Fig. 5.3(b). It has too small transmission value at the $\beta = 0$, whereas the transmission coefficient increases and stays nearly the same for the $\beta > 0.1$. This result actually points out that returning to the bound state characteristic leads to an increase in the transmission coefficient [see again Fig. 5.2(c)]. The same physics is valid for all the vacancy states observed within the MFH models. As shown in Fig. 5.2(d), the transmission coefficient for the vacancy state in the spin-up spectrum reaches its maximum at the $\beta = 0.4$, although there is a small deviation at the $\beta = 0.1$. When it comes to the vacancy state in the spin-down spectrum, the transmission coefficient [Fig. 5.2(f)] gradually increases up to the $\beta = 0.4$ when we charge the defect. The reasons for this is the regaining of the initial bound state characteristic.

CHAPTER 6

CONCLUSIONS

In this thesis, we study the electronic, magnetic, and transport properties of the GQDs in the presence of charged impurities. In this manner, we find that the lowest angular momentum channel of the hexagonal GQDs with armchair edges turns into a quasi-bound state when the Coulomb impurity is placed at the center of these GQDs, as similar to the bulk graphene. In addition, the different sized hexagonal GQDs have the same characteristic. This happens at $\beta_c = 0.5$ for the non-interacting fermions modelled by the TB approximation, and the critical value becomes $\beta_c = 0.6$ when the interactions are turned on within the extended mean-field Hubbard model. Here, the interaction induced renormalization originates from the off-site Coulomb repulsion. As for the four-fold degeneracies of these GQDs, the spin and valley degeneracies are preserved, even in the presence of the central Coulomb impurity. As a result, the interaction-induced renormalization of the critical coupling constant is the new findings in the current literature. We also calculate the effective charge of the impurity with the help of induced background charges by specifying a circle centered around the impurity. This induced charge around the impurity reduces the bare charge of the impurity to the effective charge of the impurity, and it is found that the effective charge of the impurity is $Z_{eff} \approx 1$.

We also discuss the effect of lattice distortions induced by random bare carbon vacancies and spatial potential fluctuations induced by random Gaussian impurities. When the random bare carbon vacancies are distributed, the critical coupling constant increases due to the presence of localized defect states around the FL. In addition to these lattice defects, we create potential fluctuation, which is normally caused by the substrate. The increment in β_c due to the potential fluctuations arises from rearrangements of electron-hole puddles with respect to the Coulomb field. In total, we report the increments in β_c up to %34 in the coexistence of %1 carbon vacancy and $|\Delta| < 0.5t$. This finding may explain why the Coulomb impurities are subcritical in experiments and mimics that atomic collapse can be similarly observed in the defect-rich samples, and which can be tested with hydrogenated graphene.

As for the charged vacancy, the critical coupling constant does not show up any change within the TB model, but on the other hand it is found to be $\beta_c = 0.7$ within the mean field Hubbard model. In addition, a charged vacancy can be used to adjust or modify the magnetic properties of the GQDs. As an example, the local magnetic moment can be adjusted by charging a single bare vacancy. In this manner, the spin splitting induced by a bare vacancy strongly depends on the value of the coupling strength between the charge state of the vacancy and the lattice of GQDs. When a vacancy is charged with the subcritical Coulomb potential, the spin splitting gradually decreases, and finally, it becomes to zero due to the regaining of the spin symmetry between the spin-up and spin-down fermions. On the other hand, the valley splitting in electron and hole channels continues to exist in not only the subcritical regime, but also in the supercritical regime. Such a behaviour of these degeneracies may be used to create new types of spintronic devices in the near future. In the presence of the edge states in the triangular GQDs, the charging of the vacancy has no effect on the edge spin densities. Similar to the hexagonal GQDs, the characteristic triangular shape of the bare vacancy in these GQDs gradually decreases, and then it disappears in the subcritical regime.

We also study the transmission coefficients of the lowest bound states of the different sized hexagonal GQDs within the TB and MFH models, which is in compliance with our previous findings. A direct result related to the merging of the lowest bound state below the zero energy level is discussed with the help of transmission coefficients. When the lowest bound state dives into the negative energies, its transmission coefficient in all sized hexagonal GQDs immediately decreases within both model. This means that the lowest angular momentum channel becomes the first critical state of the impurity, which alternatively explain the basic assumption in the graphene version of atomic collapse. When a vacancy is intentionally created, and then, the defect state in the energy spectrum is measured as a function of the coupling strength, we show that its transmission coefficient increases due to the regaining of original bound sate characteristic. These findings clearly explain the Coulomb impurity problem in the GQDs.

Although we have made the subject of the atomic collapse simpler and more understandable throughout this thesis, the findings in the literature are related to the perfect graphene lattice. Based on the experimental facts, an investigations of the effective charge of the impurity can be modelled in the presence of potential fluctuations, which

is missing in the current literature. The numerical calculations we have made only in the presence of random vacancies can also be repeated by defining a finite potential per atom to model the chemisorption of hydrogen on graphene lattice. On the other hand, in experiments, one can charge the vacancy, and then measure the spin splitting as a function of the coupling strength. There should be regaining of the spin symmetry due to the effect of the Coulomb potential.

REFERENCES

Akola, J., H. Heiskanen, and M. Manninen (2008). Edge−dependent selection rules in magic triangular graphene flakes. *Physical Review B 77*(19), 193410.

Altıntaş, A. and A. D. Güçlü (2018). Defect induced anderson localization and magnetization in graphene quantum dots. *Solid State Communications 281*, 44–48.

Ando, T. (2006). Screening effect and impurity scattering in monolayer graphene. *Journal of the Physical Society of Japan 75*(7), 074716–074716.

Aoki, H. and M. S. Dresselhaus (2013). *Physics of graphene*. Springer Science & Business Media.

Bacon, M., S. J. Bradley, and T. Nann (2014). Graphene quantum dots. *Particle and Particle Systems Characterization 31*(4), 415–428.

Banhart, F., J. Kotakoski, and A. V. Krasheninnikov (2011). Structural defects in graphene. *ACS Nano 5*(1), 26–41.

Bardarson, J. H., J. Tworzydło, P. Brouwer, and C. Beenakker (2007). One-parameter scaling at the dirac point in graphene. *Physical Review Letters 99*(10), 106801.

Biswas, R. R., S. Sachdev, and D. T. Son (2007). Coulomb impurity in graphene. *Physical Review B 76*(20), 205122.

Bolotin, K. I., F. Ghahari, M. D. Shulman, H. L. Stormer, and P. Kim (2009). Observation of the fractional quantum hall effect in graphene. *Nature 462*(7270), 196–199.

Bostwick, A., J. L. McChesney, K. V. Emtsev, T. Seyller, K. Horn, S. D. Kevan, and E. Rotenberg (2009). Quasiparticle transformation during a metal−insulator transition in graphene. *Physical Review Letters 103*(5), 056404.

Burson, K. M., W. G. Cullen, S. Adam, C. R. Dean, K. Watanabe, T. Taniguchi, P. Kim, and M. S. Fuhrer (2013). Direct imaging of charged impurity density in common

graphene substrates. *Nano Letters 13*(8), 3576–3580.

Çakmak, K. E., A. Altıntaş, and A. D. Güçlü (2018). Effects of random atomic disorder on the magnetic stability of graphene nanoribbons with zigzag edges. *Physical Review B 98*(11), 115428.

Chakraborty, B., K. S. Gupta, and S. Sen (2013). Effect of topological defects and coulomb charge on the low energy quantum dynamics of gapped graphene. *Journal of Physics A: Mathematical and General 46*(5), 055303.

Chen, J.-H., W. G. Cullen, C. Jang, M. Fuhrer, and E. D. Williams (2009). Defect scattering in graphene. *Physical Review Letters 102*(23), 236805.

Cowan, T., H. Backe, M. Begemann, K. Bethge, H. Bokemeyer, H. Folger, J. Greenberg, H. Grein, A. Gruppe, Y. Kido, et al. (1985). Anomalous positron peaks from supercritical collision systems. *Physical Review Letters 54*(16), 1761.

Eckmann, A., A. Felten, A. Mishchenko, L. Britnell, R. Krupke, K. S. Novoselov, and C. Casiraghi (2012). Probing the nature of defects in graphene by raman spectroscopy. *Nano Letters 12*(8), 3925–3930.

Ezawa, M. (2007). Metallic graphene nanodisks: electronic and magnetic properties. *Physical Review B 76*(24), 245415.

Fernández-Rossier, J. and J. J. Palacios (2007). Magnetism in graphene nanoislands. *Physical Review Letters 99*(17), 177204.

Freitag, N. M., L. A. Chizhova, P. Nemes-Incze, C. R. Woods, R. V. Gorbachev, Y. Cao, A. K. Geim, K. S. Novoselov, J. Burgdorfer, F. Libisch, et al. (2016). Electrostatically confined monolayer graphene quantum dots with orbital and valley splittings. *Nano Letters 16*(9), 5798–5805.

Freitag, N. M., T. Reisch, L. A. Chizhova, P. Nemes-Incze, C. Holl, C. R. Woods, R. V. Gorbachev, Y. Cao, A. K. Geim, K. S. Novoselov, et al. (2018). Large tunable valley splitting in edge−free graphene quantum dots on boron nitride. *Nature Nanotechnology 13*(5), 392–397.

González-Herrero, H., J. M. Gómez-Rodríguez, P. Mallet, M. Moaied, J. J. Palacios, C. Salgado, M. M. Ugeda, J.-Y. Veuillen, F. Yndurain, and I. Brihuega (2016). Atomic−scale control of graphene magnetism by using hydrogen atoms. *Science 352*(6284), 437–441.

Greiner, W. (2000). *Relativistic Quantum Mechanics*: *Wave Equations*, Volume 3. Springer, New York.

Grujić, M., M. Tadić, and F. Peeters (2013). *Physical Review B 87*(8), 085434.

Güçlü, A., P. Potasz, and P. Hawrylak (2010). Excitonic absorption in gate−controlled graphene quantum dots. *Physical Review B 82*(15), 155445.

Güçlü, A. D., P. Potasz, M. Korkusinski, and P. Hawrylak (2014). *Graphene Quantum Dots*. Springer, Berlin.

Hämäläinen, S. K., Z. Sun, M. P. Boneschanscher, A. Uppstu, M. Ijäs, A. Harju, D. Vanmaekelbergh, and P. Liljeroth (2011). Quantum−confined electronic states in atomically well−defined graphene nanostructures. *Physical Review Letters 107*(23), 236803.

Hashimoto, A., K. Suenaga, A. Gloter, K. Urita, and S. Iijima (2004). Direct evidence for atomic defects in graphene layers. *Nature 430*(7002), 870–873.

Katsnelson, M., K. Novoselov, and A. Geim (2006). Chiral tunnelling and the klein paradox in graphene. *Nature physics 2*(9), 620–625.

Katsnelson, M. I. and M. Iosifovich (2012). *Graphene*: *carbon in two dimensions*. Cambridge university press.

Khalilov, V. and C.-L. Ho (1998). Dirac electron in a coulomb field in (2+ 1) dimensions. *Modern Physics Letters A 13*(08), 615–622.

Kotov, V. N., V. M. Pereira, and B. Uchoa (2008). Polarization charge distribution in gapped graphene: Perturbation theory and exact diagonalization analysis. *Physical Review B 78*(7), 075433.

Kotov, V. N., B. Uchoa, and A. C. Neto (2008). Electron−electron interactions in the vacuum polarization of graphene. *Physical Review B 78*(3), 035119.

Kotov, V. N., B. Uchoa, V. M. Pereira, F. Guinea, and A. C. Neto (2012). Electron−electron interactions in graphene: Current status and perspectives. *Reviews of Modern Physics 84*(3), 1067.

Kul, E. B., M. Polat, and A. Güçlü (2020). Electronic and magnetic properties of graphene quantum dots with two charged vacancies. *Solid State Communications 322*, 114096.

Kuleshov, V. M., V. D. Mur, N. B. Narozhny, A. M. Fedotov, and Y. E. Lozovik (2015). Coulomb problem for graphene with the gapped electron spectrum. *JETP Letters 101*(4), 264–270.

Li, M., T. Chen, J. J. Gooding, and J. Liu (2019). Review of carbon and graphene quantum dots for sensing. *ACS sensors 4*(7), 1732–1748.

Li, S.-Y., Y.-N. Ren, Y.-W. Liu, M.-X. Chen, H. Jiang, and L. He (2019). Nanoscale detection of valley−dependent spin splitting around atomic defects of graphene. *2D Materials 6*(3), 031005.

Li, X., W. Cai, J. An, S. Kim, J. Nah, D. Yang, R. Piner, A. Velamakanni, I. Jung, E. Tutuc, et al. (2009). Large−area synthesis of high−quality and uniform graphene films on copper foils. *Science 324*(5932), 1312–1314.

Lu, J., H.-Z. Tsai, A. N. Tatan, S. Wickenburg, A. A. Omrani, D. Wong, A. Riss, E. Piatti, K. Watanabe, T. Taniguchi, et al. (2019). Frustrated supercritical collapse in tunable charge arrays on graphene. *Nature Communications 10*(1), 1–8.

Lucchese, M. M., F. Stavale, E. M. Ferreira, C. Vilani, M. V. d. O. Moutinho, R. B. Capaz, C. A. Achete, and A. Jorio (2010). Quantifying ion−induced defects and raman relaxation length in graphene. *Carbon 48*(5), 1592–1597.

MacDonald, A. H., J. Jung, and F. Zhang (2012). Pseudospin order in monolayer, bilayer and double-layer graphene. *Physica Scripta 2012*(T146), 014012.

Mao, J., Y. Jiang, D. Moldovan, G. Li, K. Watanabe, T. Taniguchi, M. R. Masir, F. M. Peeters, and E. Y. Andrei (2016). Realization of a tunable artificial atom at a supercritically charged vacancy in graphene. *Nature Physics 12*(6), 545–549.

Martin, J., N. Akerman, G. Ulbricht, T. Lohmann, J. v. Smet, K. Von Klitzing, and A. Yacoby (2008). Observation of electron−hole puddles in graphene using a scanning single−electron transistor. *Nature Physics 4*(2), 144–148.

McCreary, K. M., A. G. Swartz, W. Han, J. Fabian, and R. K. Kawakami (2012). Magnetic moment formation in graphene detected by scattering of pure spin currents. *Physical Review Letters 109*(18), 186604.

Meyer, J. C., C. Kisielowski, R. Erni, M. D. Rossell, M. Crommie, and A. Zettl (2008). Direct imaging of lattice atoms and topological defects in graphene membranes. *Nano Letters 8*(11), 3582–3586.

Moldovan, D. and F. Peeters (2016). Atomic collapse in graphene. In *Nanomaterials for Security*, pp. 3–17. Springer.

Mueller, M. L., X. Yan, J. A. McGuire, and L.-s. Li (2010). Triplet states and electronic relaxation in photoexcited graphene quantum dots. *Nano Letters 10*(7), 2679–2682.

Müller, W., R. Schiller, and W. Nolting (2000). *The European Physical Journal B−Condensed Matter and Complex Systems 16*(4), 705–718.

Neto, A. C., F. Guinea, N. M. Peres, K. S. Novoselov, and A. K. Geim (2009). The electronic properties of graphene. *Reviews of Modern Physics 81*(1), 109.

Novikov, D. (2007). Elastic scattering theory and transport in graphene. *Physical Review B 76*(24), 245435.

Novoselov, K. S., A. K. Geim, S. V. Morozov, D. Jiang, Y. Zhang, S. V. Dubonos, I. V. Grigorieva, and A. A. Firsov (2004). Electric field effect in atomically thin carbon films. *Science 306*(5696), 666–669.

Olle, M., G. Ceballos, D. Serrate, and P. Gambardella (2012). Yield and shape selection of graphene nanoislands grown on ni (111). *Nano Letters 12*(9), 4431–4436.

Özdemir, H. U., A. Altıntaş, and A. D. Güçlü (2016). Magnetic phases of graphene nanoribbons under potential fluctuations. *Physical Review B 93*(1), 014415.

Pereira, V. M., J. L. Dos Santos, and A. C. Neto (2008). Modeling disorder in graphene. *Physical Review B 77*(11), 115109.

Pereira, V. M., F. Guinea, J. L. Dos Santos, N. Peres, and A. C. Neto (2006). Disorder induced localized states in graphene. *Physical Review Letters 96*(3), 036801.

Pereira, V. M., V. N. Kotov, and A. C. Neto (2008). Supercritical coulomb impurities in gapped graphene. *Physical Review B 78*(8), 085101.

Pereira, V. M., J. Nilsson, and A. C. Neto (2007). Coulomb impurity problem in graphene. *Physical Review Letters 99*(16), 166802.

Polat, M. and A. Güçlü (2020). Atomic collapse in disordered graphene quantum dots. *Physical Review B 102*(17), 174204.

Polat, M., H. Sevinçli, and A. Güçlü (2020). Collapse of the vacuum in hexagonal graphene quantum dots: a comparative study between tight-binding and mean−field hubbard models. *Physical Review B 101*(20), 205429.

Pomeranchuk, I. and Y. Smorodinsky (1945). On the energy levels of systems with z > 137. *J. Phys. Ussr 9*, 97.

Ponomarenko, L. A., F. Schedin, M. I. Katsnelson, R. Yang, E. W. Hill, K. S. Novoselov, and A. K. Geim (2008). Chaotic dirac billiard in graphene quantum dots. *Science 320*(5874), 356–358.

Potasz, P., A. Güçlü, and P. Hawrylak (2010). *Physical Review B 82*(7), 075425.

Reinhardt, J. and W. Greiner (1977). Quantum electrodynamics of strong fields. *Reports on Progress in Physics 40*(3), 219.

Sarma, S. D., S. Adam, E. Hwang, and E. Rossi (2011). Electronic transport in two-dimensional graphene. *Reviews of Modern Physics 83*(2), 407.

Schnez, S., K. Ensslin, M. Sigrist, and T. Ihn (2008). Analytic model of the energy

spectrum of a graphene quantum dot in a perpendicular magnetic field. *Physical Review B 78*(19), 195427.

Schweppe, J., A. Gruppe, K. Bethge, H. Bokemeyer, T. Cowan, H. Folger, J. Greenberg, H. Grein, S. Ito, R. Schule, et al. (1983). Observation of a peak structure in positron spectra from u + cm collisions. *Physical Review Letters 51*(25), 2261.

Sheng, W.-d., M. Korkusinski, A. D. Güçlü, M. Zielinski, P. Potasz, E. S. Kadantsev, O. Voznyy, and P. Hawrylak (2012). Electronic and optical properties of semiconductor and graphene quantum dots. *Frontiers of Physics 7*(3), 328–352.

Shytov, A., M. Katsnelson, and L. Levitov (2007a). Atomic collapse and quasi−rydberg states in graphene. *Physical Review Letters 99*(24), 246802.

Shytov, A. V., M. I. Katsnelson, and L. S. Levitov (2007b). Vacuum polarization and screening of supercritical impurities in graphene. *Physical Review Letters 99*(23), 236801.

Su, J., M. Telychko, P. Hu, G. Macam, P. Mutombo, H. Zhang, Y. Bao, F. Cheng, Z.-Q. Huang, Z. Qiu, et al. (2019). Atomically precise bottom-up synthesis of π-extended [5] triangulene. *Science Advances 5*(7), eaav7717.

Subramaniam, D., F. Libisch, Y. Li, C. Pauly, V. Geringer, R. Reiter, T. Mashoff, M. Liebmann, J. Burgdörfer, C. Busse, et al. (2012). Wave−function mapping of graphene quantum dots with soft confinement. *Physical Review Letters 108*(4), 046801.

Terekhov, I. S., A. I. Milstein, V. N. Kotov, and O. P. Sushkov (2008). Screening of coulomb impurities in graphene. *Physical Review Letters 100*(7), 076803.

Torres, L. E. F., S. Roche, and J.-C. Charlier (2020). *Introduction to graphene−based nanomaterials*: *from electronic structure to quantum transport*. Cambridge University Press.

Ugeda, M., D. Fernández-Torre, I. Brihuega, P. Pou, A. Martínez-Galera, R. Pérez, and

J. Gómez-Rodríguez (2011). Point defects on graphene on metals. *Physical Review Letters 107*(11), 116803.

Ugeda, M. M., I. Brihuega, F. Guinea, and J. M. Gómez-Rodríguez (2010). Missing atom as a source of carbon magnetism. *Physical Review Letters 104*(9), 096804.

Van Pottelberge, R., M. Zarenia, P. Vasilopoulos, and F. Peeters (2017). Graphene quantum dot with a coulomb impurity: subcritical and supercritical regime. *Physical Review B 95*(24), 245410.

Vozmediano, M. A. and F. Guinea (2012). Effect of coulomb interactions on the physical observables of graphene. *Physica Scripta 2012*(T146), 014015.

Wang, W.-X., Y.-W. Wei, S.-Y. Li, X. Li, X. Wu, J. Feng, and L. He (2018). Imaging the dynamics of an individual hydrogen atom intercalated between two graphene sheets. *Physical Review B 97*(8), 085407.

Wang, Y., V. W. Brar, A. V. Shytov, Q. Wu, W. Regan, H.-Z. Tsai, A. Zettl, L. S. Levitov, and M. F. Crommie (2012). Mapping dirac quasiparticles near a single coulomb impurity on graphene. *Nature Physics 8*(9), 653–657.

Wang, Y., D. Wong, A. V. Shytov, V. W. Brar, S. Choi, Q. Wu, H.-Z. Tsai, W. Regan, A. Zettl, R. K. Kawakami, et al. (2013). Observing atomic collapse resonances in artificial nuclei on graphene. *Science 340*(6133), 734–737.

Wimmer, M., A. Akhmerov, and F. Guinea (2010). Robustness of edge states in graphene quantum dots. *Physical Review B 82*(4), 045409.

Wong, D., F. Corsetti, Y. Wang, V. W. Brar, H.-Z. Tsai, Q. Wu, R. K. Kawakami, A. Zettl, A. A. Mostofi, J. Lischner, et al. (2017). Spatially resolving density-dependent screening around a single charged atom in graphene. *Physical Review B 95*(20), 205419.

Yazdi, G. R., T. Iakimov, and R. Yakimova (2016). Epitaxial graphene on sic: a review of growth and characterization. *Crystals 6*(5), 53.

Yazyev, O. V. (2010). Emergence of magnetism in graphene materials and

nanostructures. *Reports on Progress in Physics 73*(5), 056501.

Yazyev, O. V. and L. Helm (2007). Defect−induced magnetism in graphene. *Physical Review B 75*(12), 125408.

Zarenia, M., A. Chaves, G. Farias, and F. Peeters (2011). Energy levels of triangular and hexagonal graphene quantum dots: a comparative study between the tight−binding and dirac equation approach. *Physical Review B 84*(24), 245403.

Zeldovich, Y. B. and V. S. Popov (1972). Electronic structure of superheavy atoms. *Soviet Physics Uspekhi 14*(6), 673.

Zhang, Y., V. W. Brar, C. Girit, A. Zettl, and M. F. Crommie (2009). Origin of spatial charge inhomogeneity in graphene. *Nature Physics 5*(10), 722–726.

Zhang, Y., S.-Y. Li, H. Huang, W.-T. Li, J.-B. Qiao, W.-X. Wang, L.-J. Yin, K.-K. Bai, W. Duan, and L. He (2016). Scanning tunneling microscopy of the π magnetism of a single carbon vacancy in graphene. *Physical Review Letters 117*(16), 166801.

Zhou, L. (2017). Notes on steady state current through a noninteracting quantum dot. *arXiv:1704.04733*.

Zhou, S. Y., G.-H. Gweon, A. Fedorov, d. First, PN, W. De Heer, D.-H. Lee, F. Guinea, A. C. Neto, and A. Lanzara (2007). Substrate−induced bandgap opening in epitaxial graphene. *Nature Materials 6*(10), 770–775.

Zhu, W., Z. Wang, Q. Shi, K. Szeto, J. Chen, and J. Hou (2009). Electronic structure in gapped graphene with a coulomb potential. *Physical Review B 79*(15), 155430.

VITA

Date and Place of Birth: 01.09.1987, Yozgat-TURKEY

EDUCATION

2013 - 2019 Doctor of Philosophy in Department of Physics

Graduate School of Engineering and Sciences, İzmir Institute of Technology, İzmir -Turkey

Thesis Title: Electronic, Magnetic and Transport Properties of Graphene Quantum Dots with Charged Impurities

Supervisor: Prof. Dr. Alev Devrim Güçlü

2011 - 2013 Master of Science in Physics

Graduate School of Engineering and Sciences, İzmir Institute of Technology, İzmir -Turkey

Thesis Title: Characterization of GaAs (211) Surface for Epitaxial Buffer Growth

Supervisor: Assoc. Dr. Yusuf Selamet

SELECTED PUBLICATIONS

Arı, O. and Polat, M. and Karakaya, M. and Selamet, Y.
(2015). "Growth and characterization of CdTe absorbers on GaAs by MBE for high concentration PV solar cells".
Physica Status Solidi (c), 12(9-11), 1211.

Polat, M., Arı, O., Öztürk, O. and Selamet, Y.
(2017). "Reciprocal space mapping study of CdTe epilayer grown by molecular beam epitaxy on (2 1 1) B GaAs substrate".
Materials Research Express, 4(3), 035904.

Polat M., Bilgilisoy E., Arı O., Öztürk O. and Selamet Y.

(2018). "Identifying threading dislocations in CdTe films by reciprocal space mapping and defect decoration etching".
Journal of Applied Physics, 124(8), 085710.

Polat M., Sevinçli H. and Güçlü A. D.
(2020). "Collapse of the vacuum in hexagonal graphene quantum dots: A comparative study between tight-binding and mean-field Hubbard models".
Physical Review B, 101(20), 205429.

Kul, E. B., Polat M. and Güçlü A. D.
(2020). "Electronic and magnetic properties of graphene quantum dots with two charged vacancies".
Solid State Communications, 322, 114096.

Polat M. and Güçlü A. D.
(2020). "Atomic collapse in disordered graphene quantum dots".
Physical Review B, 102(17), 174204.

Permanent Address: İzmir